

RESEARCH ARTICLE

TNF α -induced metabolic reprogramming drives an intrinsic anti-viral stateJessica Ciesla, Isreal Moreno, Jr., Joshua Munger *

Department of Biochemistry and Biophysics, University of Rochester School of Medicine and Dentistry, Rochester, New York, United States of America

* Joshua_Munger@urmc.rochester.edu

Abstract

Cytokines induce an anti-viral state, yet many of the functional determinants responsible for limiting viral infection are poorly understood. Here, we find that TNF α induces significant metabolic remodeling that is critical for its anti-viral activity. Our data demonstrate that TNF α activates glycolysis through the induction of hexokinase 2 (HK2), the isoform predominantly expressed in muscle. Further, we show that glycolysis is broadly important for TNF α -mediated anti-viral defense, as its inhibition attenuates TNF α 's ability to limit the replication of evolutionarily divergent viruses. TNF α was also found to modulate the metabolism of UDP-sugars, which are essential precursor substrates for glycosylation. Our data indicate that TNF α increases the concentration of UDP-glucose, as well as the glucose-derived labeling of UDP-glucose and UDP-N-acetyl-glucosamine in a glycolytically-dependent manner. Glycolysis was also necessary for the TNF α -mediated accumulation of several glycosylated anti-viral proteins. Consistent with the importance of glucose-driven glycosylation, glycosyl-transferase inhibition attenuated TNF α 's ability to promote the anti-viral cell state. Collectively, our data indicate that cytokine-mediated metabolic remodeling is an essential component of the anti-viral response.

 OPEN ACCESS

Citation: Ciesla J, Moreno I, Jr., Munger J (2022) TNF α -induced metabolic reprogramming drives an intrinsic anti-viral state. *PLoS Pathog* 18(7): e1010722. <https://doi.org/10.1371/journal.ppat.1010722>

Editor: Deborah Lenschow, Washington University in Saint Louis, UNITED STATES

Received: March 7, 2022

Accepted: July 1, 2022

Published: July 14, 2022

Copyright: © 2022 Ciesla et al. This is an open access article distributed under the terms of the [Creative Commons Attribution License](https://creativecommons.org/licenses/by/4.0/), which permits unrestricted use, distribution, and reproduction in any medium, provided the original author and source are credited.

Data Availability Statement: All relevant data are within the manuscript and its [Supporting Information](#) files.

Funding: The work was also supported by NIH grants AI127370 and AI50698 to J.M. J.C. and I.M. were supported by an NIH T32 Training Grant (GM068411). J.C. was also supported by a NIH T32 Training Grant in HIV Replication and Pathogenesis (AI1049815). This research has been facilitated by the services provided by the University of Rochester Mass Spectrometry Resource Laboratory and NIH instrument grant

Author summary

Viral infection often activates a host cell's intrinsic immune response resulting in the cellular secretion of cytokines, important host-defense molecules. These cytokines act on neighboring cells to make them less permissive to viral infection. Many of the mechanisms through which cytokines promote a less permissive cell state remain unclear. Our data indicate that treatment with the anti-viral cytokine TNF α induces substantial changes to cellular metabolic activity, including activating glucose metabolism. We find that these TNF α -induced metabolic changes are critical for TNF α to limit the replication of diverse viruses including Human Cytomegalovirus and two Coronaviruses, OC43 and SARS-CoV-2. Inhibition of glucose metabolism during TNF α treatment prevented the expression of a variety of known cellular anti-viral proteins. Collectively, our data indicate that cytokine-induced metabolic remodeling is an important component of TNF α 's ability to promote a less permissive cell state and raises further questions about the mechanisms

(S100D025242). The funders had no role in study design, data collection and analysis, decision to publish, or preparation of the manuscript.

Competing interests: The authors have declared that no competing interests exist.

through which specific cytokine-induced metabolic activities contribute to various aspects of anti-viral defense.

Introduction

Viruses are obligate intracellular parasites that cause substantial human morbidity and mortality. Newly emergent viruses can cause pandemics, for example, SARS-CoV-2, which in 2020 was the 3rd leading cause of death in the U.S with ~375,000 deaths [1]. In contrast, endemic viruses frequently present a lower, but constant burden to human health. Human Cytomegalovirus (HCMV), an endemic β -Herpesvirus, causes severe disease in various immunosuppressed populations, including the elderly, cancer patients receiving immunosuppressive chemotherapy, transplant recipients, and AIDS patients [2,3]. HCMV is also a major source of congenital birth defects. In the United States alone, 1 in 200 babies are born with congenital HCMV and one out of five of these newborns exhibit long-term health problems including microcephaly, deafness, or retinitis [4].

Prevention of virally-associated morbidity requires a strong innate immune response [5]. These responses are frequently initiated through viral antigen recognition by cellular pattern recognition receptors (PRRs) that activate signal transduction cascades, and ultimately trigger the production of anti-viral cytokines, including Tumor Necrosis Factor- α (TNF α), Types 1, 2, and 3 Interferons (IFNs), and interleukins (ILs) [5]. These cytokines are critical for recruiting tissue-resident and circulating immune cells to the site of infection [6,7], but importantly, they also induce an anti-viral state in uninfected bystander cells [8,9]. TNF α , for example, inhibits the replication of a variety of evolutionarily diverse viruses including Vesicular Stomatitis virus (VSV), Encephalomyocarditis virus (EMCV), Herpes Simplex virus (HSV) [10], HCMV [11], and Hepatitis C virus (HCV) [12]. For many cytokine-induced signaling pathways, much of the upstream signaling network has been elucidated, e.g., cytokine-receptor binding ultimately resulting in transcription factor activation and expression of cytokine-associated genes [13–15]. However, much less is known about the cellular biology associated with the institution of the anti-viral state. For example, while several cytokine-induced genes have been found to be important for intrinsic immune defense [15], how these genes modulate normal cellular physiology to limit infection is largely unclear.

Metabolic reprogramming has emerged as a central feature of the functional responses of professional immune cells. For example, glycolytic regulation is important for B cell function [16,17], and aspects of fatty acid and mitochondrial metabolism are critical for T cell activation and the maintenance of memory T cells [18,19]. Similarly, granulocytes, monocytes, and macrophages have all been found to rely on aspects of glycolytic and glutaminolytic metabolism to differentiate, polarize, infiltrate infected tissues, and phagocytose infected cells [20–24]. While metabolic remodeling in professional innate and adaptive immune cells has emerged as a critical component of a successful immune response, surprisingly little is known about how cytokine signaling impacts the metabolism of non-professional bystander cells or the potential role that cytokine-induced metabolic modulation contributes to limiting viral infection.

Here, we apply metabolomic approaches to elucidate how TNF α modulates cellular metabolism to support its anti-viral activity. We find that TNF α induces HK2 to activate glycolysis, and that TNF α -activated glycolysis funnels carbon towards UDP-sugar biosynthesis. Restricting glycolysis largely blocks TNF α 's ability to limit the replication of HCMV and two betacoronaviruses, OC43 and SARS-CoV-2. This loss of anti-viral activity coincides with substantially decreased expression of several intrinsic anti-viral factors, several of which are glycosylated.

Consistent with an important role for glycosylation, we find that inhibition of glycosyltransferases also inhibits TNF α 's anti-viral activity. Together, our data indicate that TNF α -induced glycolysis promotes UDP-sugar turnover to support glycosylation, which is required for the expression of intrinsic anti-viral factors and the induction of an anti-viral cellular state.

Results

TNF α induces glycolysis as part of a broadly altered metabolic state

To elucidate how TNF α treatment impacts cellular metabolism, we employed LC-MS/MS to analyze cellular metabolic pools in vehicle-treated non-transformed human foreskin fibroblasts (HFFs) versus those treated with TNF α (S1 Table). Principal-component analysis (PCA) of the resulting data discriminated between vehicle and TNF α -treated samples in the first principal component (Fig 1A). Further, hierarchical clustering of these data segregated TNF α treated samples from control samples (Fig 1B). Together, these data suggest that TNF α treatment induces a distinct metabolic state. The relative abundance of twelve metabolites were significantly altered by TNF α treatment (Fig 1C and S2 Table). Notably, the largest metabolite increase was in kynurenine abundance, which was ~20-fold more abundant in TNF α -treated cells relative to control (Fig 1C). Kynurenine is part of the tryptophan catabolic pathway that supports NAD⁺ biosynthesis [25,26], however, in this study NAD⁺ pools were significantly decreased upon TNF α treatment (Fig 1C). Intriguingly, a similar response, i.e., increased kynurenine and decreased NAD⁺ levels, was recently shown to occur after inflammatory challenge in macrophages, and subsequently found to be important for proper innate immune responses [27]. In addition, two of the most significantly increased metabolites, ribose-phosphate and sedoheptulose-7-phosphate, are part of the pentose phosphate pathway (Fig 1C and 1D). Hexose-phosphate was also significantly increased by TNF α treatment (Fig 1C and 1D), as was UDP-glucose, a key glycosylation precursor and glycogen building block (Fig 1C and 1D).

Given TNF α 's impact on glycolytic and pentose phosphate metabolite abundances, we more thoroughly investigated the impact of TNF α treatment on metabolites from these pathways (Fig 1D) over a time course. TNF α treatment substantially increased several glycolytic metabolite pools over multiple time points (Fig 2A and S3 Table). Four hours after TNF α treatment, the levels of fructose-1,6-bisphosphate, whose production is one of the rate-determining steps of glycolysis [28], more than doubled. Other glycolytic pools were induced by TNF α treatment at multiple time points including fructose-6-phosphate, dihydroxyacetone phosphate, and glyceraldehyde-3-phosphate (Fig 2A). Similarly, UDP-glucose of the hexosamine pathway was induced at 12 and 24 hours (Fig 2A). For pentose phosphate metabolites: sedoheptulose-7-phosphate was only induced at 24 hours post-TNF α treatment, whereas ribose-phosphate was induced at all time points analyzed (Fig 2A).

The steady-state elevation of several glycolytic intermediates suggested that TNF α -treatment may induce glycolysis. To test this possibility, we analyzed the impact of TNF α on glucose consumption and lactate secretion, which were both substantially induced by TNF α treatment (Fig 2B and 2C). Treatment with 2-deoxyglucose (2DG), a glycolytic inhibitor, diminished basal levels of glycolysis and strongly inhibited TNF α -mediated glycolytic activation as shown by reduced lactate secretion compared to vehicle-treated samples (Fig 2C). Collectively, our data indicate that TNF α treatment promotes significant metabolic alterations and drives glycolytic induction.

TNF α -mediated glycolytic activation is important for its anti-viral activity

To examine how glycolytic inhibition impacted TNF α -induced metabolic modulation, we analyzed the metabolomic impact of 2DG co-treatment with TNF α via LC-MS/MS (S4 Table).

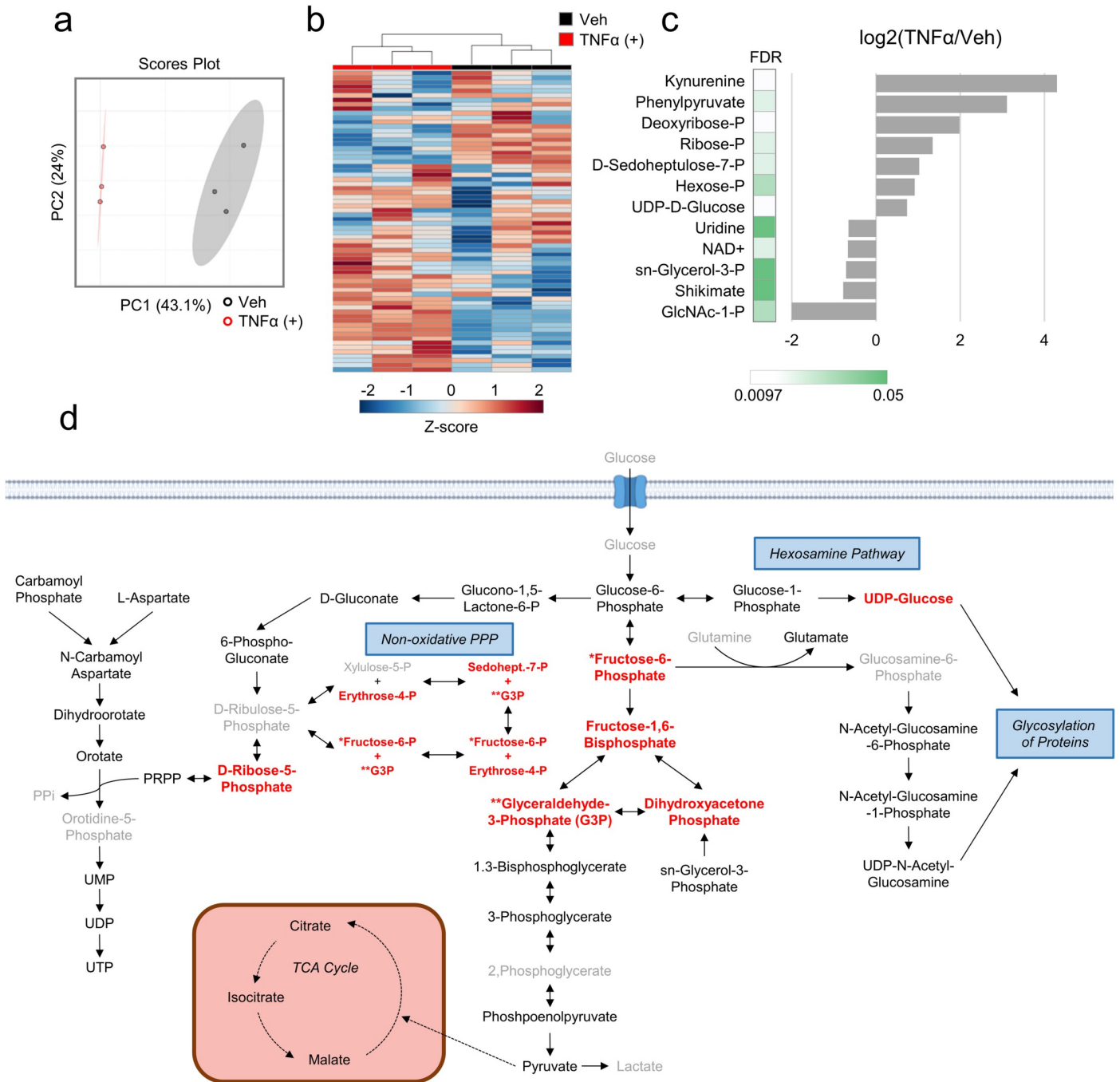


Fig 1. TNF α treatment induces broad metabolic changes. (a-c) HFFs were treated with TNF α (10 ng/mL, red) or vehicle (black) for 24 hr. Metabolites were extracted from cells and analyzed by LC-MS/MS as indicated in the materials and methods (n = 3). **a** Principal component analysis (PCA) of metabolite data. **b** Hierarchical clustering of metabolite data depicted as Z-scores from min (blue) to max (red). **c** Metabolites significantly altered by TNF α treatment. **d** Schematic representing metabolites in pathways of interest. Metabolites depicted in black are experimentally detected, whereas those in grey are not detected. Metabolites in red are significantly more abundant in at least one time point during 24 hours of TNF α treatment (Fig 2A). Solid lines represent a direct metabolic conversion while dashed lines represent an indirect conversion. Single headed arrows represent an irreversible reaction, double headed arrows represent a reversible reaction.

<https://doi.org/10.1371/journal.ppat.1010722.g001>

PCA indicated that the largest amount of data variance, i.e., 37.1% of the variance associated with PC1, separated all 2DG treated from the non-2DG treated samples regardless of TNF α

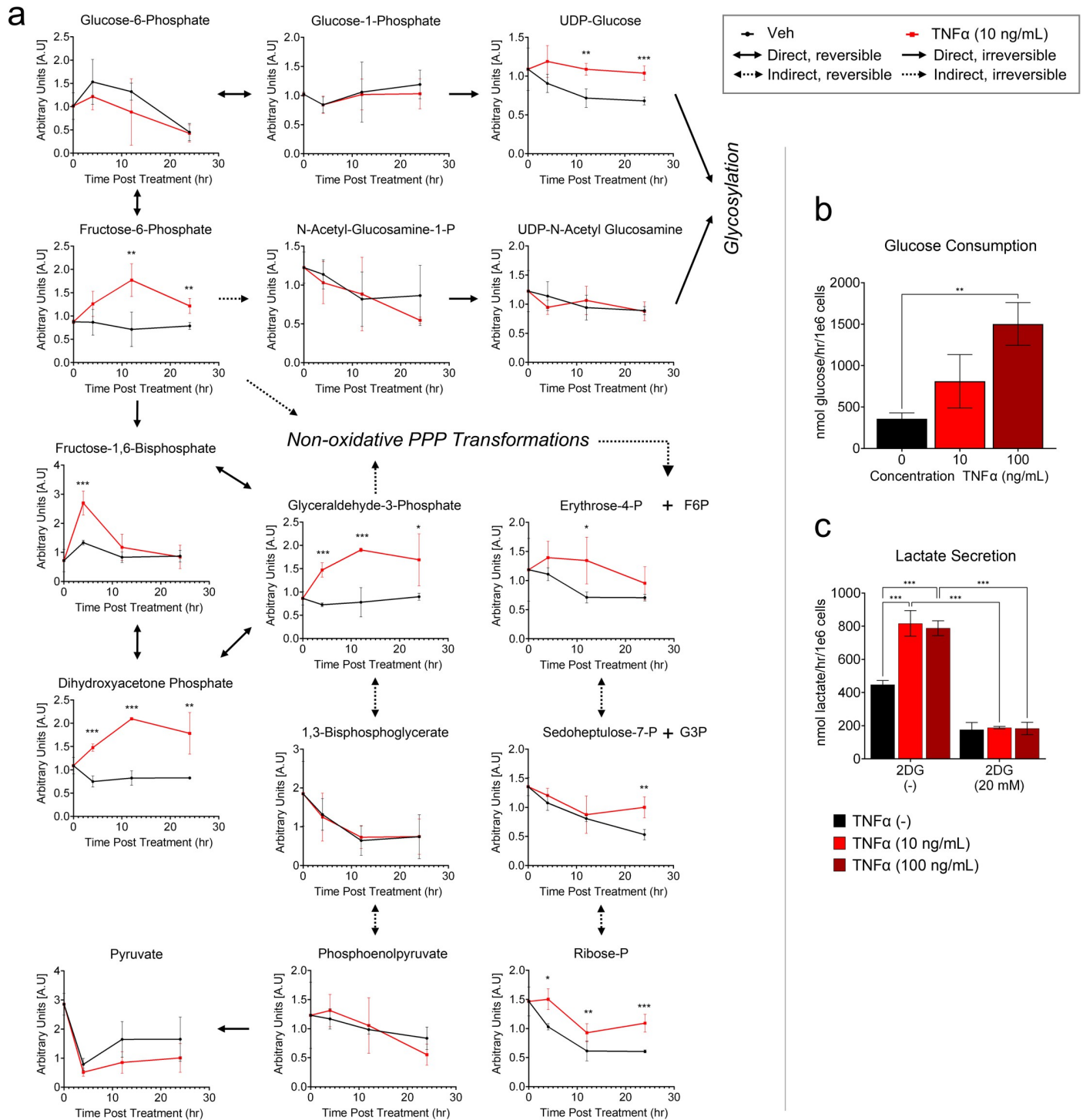


Fig 2. TNF α treatment induces glycolytic flux. **a** HFFs were treated with TNF α (10 ng/mL, red) or vehicle (black) for 0, 4, 12 and 24 hr prior to metabolite extraction and downstream LC-MS/MS analysis (mean \pm SD, n = 3). For each metabolite/time point analyzed, vehicle and TNF α treated groups were compared using student's unpaired two-tailed t-test (*t<0.1, **t<0.05, ***t<0.01). Solid arrows represent direct metabolite conversions while dashed arrows represent indirect conversions. Single-headed arrows represent irreversible conversions while double-headed arrows represent reversible conversions. **(b/c)** HFFs were treated with TNF α (10 ng/mL, light red or 100 ng/mL, dark red) or vehicle (black) for 24 hr. Media harvested from each sample were analyzed for **b** glucose consumption and **c** lactate secretion. (mean \pm SD, n = 3, with FDR adjusted ANOVA p-values, *p<0.05, **p<0.01, ***p<0.001).

<https://doi.org/10.1371/journal.ppat.1010722.g002>

treatment (Fig 3A). In the non-2DG treated samples, TNF α treated samples were separated from non-TNF α treated samples along PC2 (Fig 3A). In contrast, co-treatment with 2DG largely collapsed this separation between TNF α treated and non-TNF α treated samples along PC2 (Fig 3A). Similarly, hierarchical clustering of the metabolic data primarily separated samples based on whether they were 2DG treated or not (Fig 3B). Further, as would be expected, 2DG treatment reversed the TNF α -mediated induction in glycolytic pools' sizes (Fig 3B, Cluster I, and 3C) and lactate secretion (Fig 2C).

To determine how TNF α -mediated glycolytic activation contributes to its ability to induce the anti-viral state, we assessed how glycolytic inhibition impacted TNF α 's ability to limit viral infection of the laboratory strain of HCMV, AD169. For these experiments, cells were pretreated with TNF α alone, or in combination with 2DG, for 24h prior to removing all compounds and infecting cells in medium without any compounds. Pretreatment of cells with TNF α largely blocked the ability of HCMV to initiate infection in HFFs (Fig 3D and 3E). TNF α pretreatment in the presence of 2DG largely restored the ability of HCMV to infect cells (Fig 3D and 3E). We also found that glucose starvation during TNF α pretreatment significantly increased the ability of HCMV to infect cells compared to TNF α pretreatment in glucose-containing medium (Fig 3D). Pretreatment with TNF α prior to infection at a high multiplicity of infection (MOI = 3.0) substantially reduced the accumulation of HCMV proteins throughout infection (Fig 3F). Similar to the initiation experiments, TNF α pretreatment in the presence of 2DG partially restored HCMV protein expression (Fig 3F). These results suggest that TNF α 's ability to promote an anti-viral cell state against HCMV relies on glucose availability and glycolytic flux.

To test how broadly TNF α relies on glycolysis for its antiviral activity in different cell types, we assessed AD169 infection in MRC5 lung fibroblasts, and TB40/e infection, a more recently derived clinical isolate of HCMV, in ARPE-19 retinal epithelial cells. Pretreatment with TNF α was sufficient to restrict AD169 and TB40/e infection in MRC5 and ARPE19 cell types, respectively, and restricting glycolysis with 2DG during TNF α pretreatment largely restored the ability of HCMV to initiate infection as in our original model with AD169 and HFFs (Fig 3G). Collectively, these data indicate that TNF α relies on glycolysis to induce an anti-viral state in multiple different cell types.

Given that TNF α is broadly anti-viral, we next sought to determine if TNF α 's effects on glycolysis were specific to limiting HCMV infection, or if a similar phenotype could be observed in the context of evolutionary divergent viruses. To address this question, we analyzed the replication of two β -Coronaviruses, OC43 and SARS-CoV-2 in HFFs or HFFs transduced with the angiotensin-converting enzyme 2 (ACE2), the surface protein required for SARS-CoV-2 entry [29], respectively. TNF α pretreatment was sufficient to restrict the RNA accumulation of both OC43 and SARS-CoV-2 (Fig 3H and 3I). TNF α pretreatment in the presence of 2DG largely restored OC43 and SARS-CoV-2 RNA accumulation (Fig 3H and 3I). These data align with the results from HCMV infection and support that TNF α treatment broadly requires glycolysis for its anti-viral activity.

Hexokinase 2 contributes to TNF α -mediated glycolytic activation

To obtain a complimentary picture of TNF α -induced metabolic changes and how glycolysis affects these changes, we analyzed the impact of TNF α treatment in the presence or absence of 2DG on the proteome. The abundances of 3,780 unique proteins were identified in this study (S5 Table). From this list, we extracted those involved in metabolism to study the differences in the abundance of metabolic enzymes between vehicle and TNF α treated cells. Of the 562 metabolic enzymes detected in our study, 40 were significantly more abundant as a

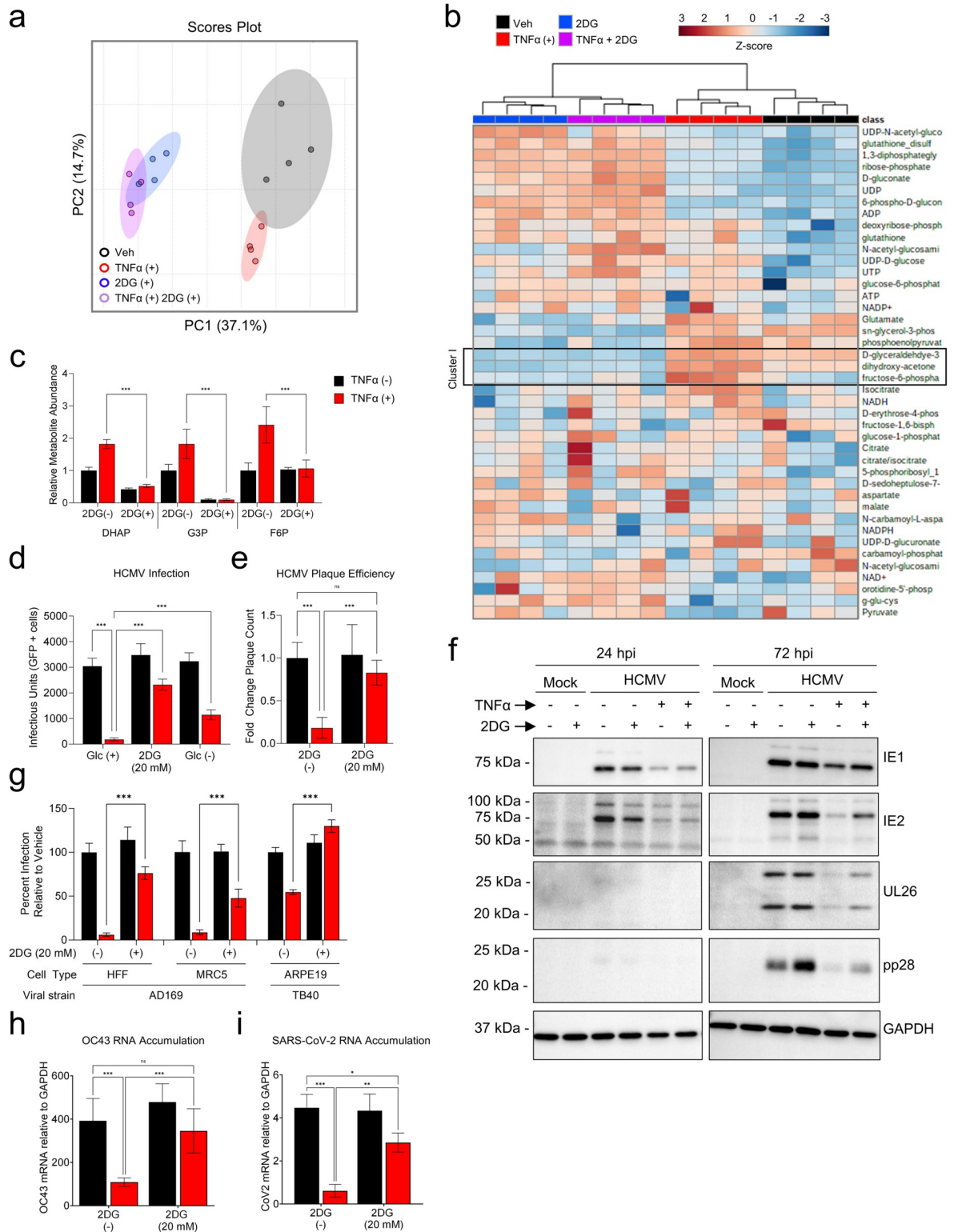


Fig 3. Glycolytic flux is required for TNFα to induce its anti-viral state. (a-c) HFFs treated with TNFα (10 ng/mL, red), 2DG (20 mM, blue), TNFα+2DG (purple), or vehicle (black) for 24 hr (n = 4). Metabolites extracted from cells and analyzed by LC-MS/MS (mean ± SD, n = 4). Metabolite data analyzed via a PCA or b Hierarchical clustering with metabolite values depicted as Z-scores from min (blue) to max (red). c Relative abundance of indicated metabolite. d HFFs treated with TNFα (10 ng/mL, red) in the presence or absence of glucose (Glc ±) or 2-deoxyglucose (2DG, 20 mM) for 24 hr prior to a media change with fresh viral adsorption media containing glucose, but without

inhibitors, and HCMV-GFP (MOI = 0.5). Infected cells were identified by GFP expression 24 hr post-infection and quantified (mean \pm SD, $n = 12$). **e** HFFs pretreated for 24 hr prior to media change with fresh viral adsorption, but without inhibitors, and a known number of HCMV-GFP infectious particles. Viral plaques were quantified ($n = 6$, relative mean \pm SD). **f** Cells were pre-treated as in **(e)**, infected with HCMV (MOI = 3), and processed for western analysis at the indicated times post-infection. **g** HFF, MRC5, and ARPE19 cells were treated as described in **(e)** prior to infection with HCMV-GFP (AD169, MOI = 0.5) or clinical strain of HCMV, TB40, containing mCherry (MOI = 0.02) as indicated. Infected HFFs and MRC5s were identified by GFP expression 24 hr post-infection and infected ARPE-19s were identified by mCherry expression 72 hr post-infection. Percent infection relative to vehicle was calculated for each cell type as described in materials and methods (mean \pm SD, $n = 6$). **h** Wild-type HFFs or **i** HFFs transduced with ACE2 were pretreated as in **(e)** prior to infection with **h** OC43 (MOI = 3) or **i** SARS-CoV-2 (MOI = 0.01) and harvested 48 hr post-infection for RT-qPCR analysis (mean \pm SD, $n = 6$ (**h**) or $n = 3$ (**i**)). (**c-e,g-i**) p -values were calculated using two-way ANOVA and FDR corrected; * $p < 0.05$, ** $p < 0.01$, *** $p < 0.001$.

<https://doi.org/10.1371/journal.ppat.1010722.g003>

result of TNF α treatment (S6 Table). Hierarchical clustering (Fig 4A) and PCA (S1 Fig) of this subset of metabolic enzymes separated TNF α -treated samples from vehicle-treated samples, suggesting that TNF α treatment substantially impacts the expression of metabolically categorized proteins. Major contributors to this shift included solute carrier family 2, facilitated glucose transporter member 1 (SLC2A1, the ubiquitous GLUT1 glucose transporter), and hexokinase-2 (HK2), the muscle predominant form of hexokinase (Fig 4A and 4B), both of which are proteins involved in glucose metabolism/glycolysis. HK2 protein was induced ~ 2.5 fold in TNF α -treated samples relative to vehicle (Fig 4C). Likewise, HK2 RNA was also substantially induced upon TNF α treatment (Fig 4D). TNF α -treatment induced GLUT1 RNA (Fig 4E), as well as GLUT1 protein (Fig 4F and 4G). Notably, 2DG treatment prevented the TNF α -mediated accumulation of GLUT1 bands (Fig 4F). These bands have previously been found to be glycoforms of GLUT1, whose accumulation is dependent on glycosyltransferase activity [30]. Further, GLUT1 RNA levels remained elevated upon co-treatment with TNF α and 2DG (Fig 4E), suggesting the loss of these GLUT1 glycoforms appears to be post-transcriptional. We hypothesized that the loss of these GLUT1 glycoforms might reflect reduced glycosyltransferase activity. To explore this possibility we treated cells with TNF α and either Kifunensine (kif), an inhibitor of N-linked glycosylation [30], or with Benzyl- α -GalNAc (BGNac), an inhibitor of O-linked glycosylation [31,32]. While the N-linked and O-linked glycosyltransferase inhibitors had slightly different impacts on TNF α -induced GLUT1 glycoform accumulation (Fig 4F), treatment with either BGNac or kif substantially reduced the expression of glycosylated GLUT1 isoforms (Fig 4F), consistent with the possibility that 2DG may be inhibiting the glycosylation of GLUT1. Additionally, 2DG treatment did not impact the accumulation of total GLUT1 peptide levels (Fig 4G), suggesting the loss of GLUT1 glycoforms is not a result of decreased GLUT1 protein expression, and consistent with 2DG treatment causing a defect in post-translational GLUT1 glycosylation. While 2DG cotreatment with TNF α reduced the accumulation of GLUT1 glycoforms, neither TNF α treatment alone nor in combination with 2DG, BGNac, or kif, impacted the total abundance of glycoproteins in the cell (S2 Fig).

In contrast to GLUT1 and HK2, no other glycolytic enzymes were significantly increased as a result of TNF α treatment, however, PFK-M and TIGAR levels were significantly reduced by TNF α treatment (Fig 4B and 4C). We also sought to examine if TNF α could be inducing Hif1 α expression given its role as a glycolysis activator [33]. While Hif1 α was not detected in the proteomics data set after 24 hours of TNF α treatment, its mRNA levels were induced 2-fold at 8 hours post-TNF α treatment relative to vehicle-treated samples (Fig 4H).

Given that HK2 is the muscle-predominant hexokinase isoform, and is not thought to be substantially expressed in fibroblasts, we sought to determine the importance of TNF α -induced expression of this isoform for glycolytic activation. We targeted HK2 and HIF1 α via CRISPR-Cas9 to assess their contributions to TNF α -mediated glycolytic activation and

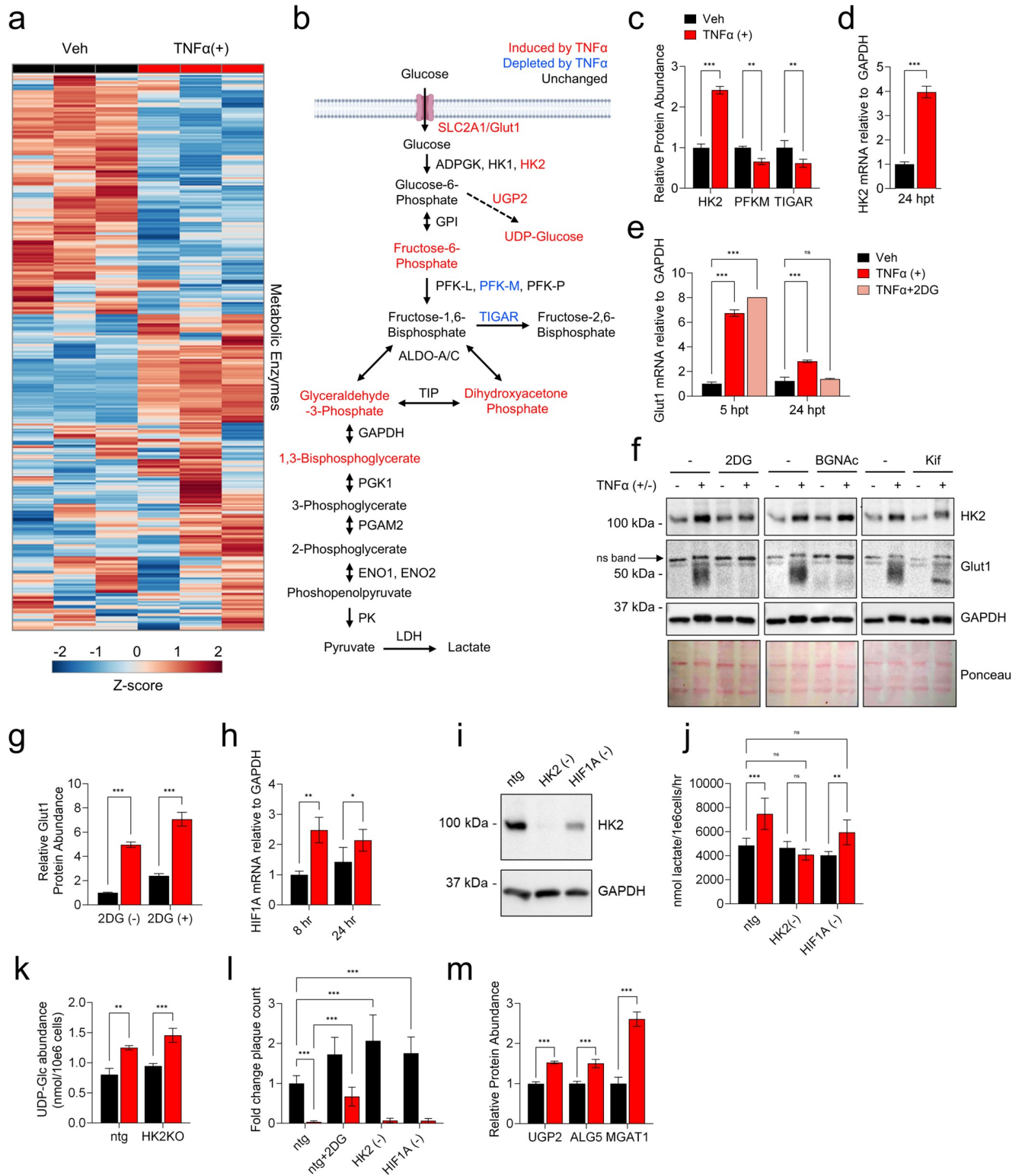


Fig 4. TNF α treatment induces HK2 expression to support glycolytic flux. HFFs were treated with TNF α (10 ng/mL, red) or vehicle (black) for 24 hr, unless otherwise indicated. **(a/c/g/m)** Cells were harvested for proteomics analysis. **a** Hierarchical clustering of proteins involved in metabolism. Protein abundance values are depicted as Z-scores from min (blue) to max (red). **b** Schematic of metabolites and enzymes involved in glycolysis significantly dysregulated by TNF α treatment at 24 hr. Red = significantly more abundant, blue = significantly less abundant. **c** Relative protein abundance of HK2, PFK-M and TIGAR normalized to vehicle-treated (mean \pm SD, n = 3). **(d/e/h)** RNA was extracted from cells at the indicated times post treatment for RT-

qPCR analysis of **d** HK2, **e** Glut1 and **h** HIF1A mRNA. **f** Cells were treated with 2DG (20 mM), Benzyl- α -GalNAc (15 mM) or Kifunensine (5 μ M) in the presence or absence of TNF α for 24 hr and analyzed by immunoblot for Glut1 and HK2 protein. (**h-l**) HFFs treated with CRISPR Cas9-RNP containing guides for HK2, HIF1A, or a non-target guide (ntg) to generate knockout (KO) cell lines. KO cells harvested for **i** immunoblot analysis. **j** Media harvested from KO cells treated as indicated for 24 hr, analyzed for lactate secretion by LC-MS/MS. **k** Metabolites extracted from KO cells treated as indicated, UDP-glucose intracellular abundance quantified using LC-MS/MS. **l** KO cells pre-treated as indicated prior to media change with fresh viral adsorption media, without inhibitors, containing a known number of HCMV-GFP infectious particles. Viral plaques were quantified and plotted as indicated. **m** Relative protein abundance of UTP-glucose-1-phosphate uridylyl transferase (UGP2), Dolichyl-phosphate beta-glucosyltransferase (ALG5), and Alpha-1,3-mannosyl-glycoprotein 2-beta-N-acetylglucosamine transferase (MGAT1) (mean \pm SD, n = 3). **d** mean \pm SD, n = 3, two-tailed unpaired ttest, *p<0.05, **p<0.01, ***p<0.001. **c/g/h/m** mean \pm SD, n = 3; **e/k** mean \pm SD, n = 2; **j** mean \pm SD, n = 4; **l** mean \pm SD n = 15; with FDR-adjusted p-values determined using 2-way ANOVA followed by two-stage step-up method of Benjamini, Krieger and Yekutieli *p<0.05, **p<0.01, ***p<0.001.

<https://doi.org/10.1371/journal.ppat.1010722.g004>

induction of an anti-viral cell state. RNP-based Cas9 delivery successfully inactivated HK2, resulting in the loss of HK2 protein accumulation (Fig 4I). While Hif1 α protein could not be detected by western blot, genomic ablation of the HIF1A gene was confirmed via genomic sequence analysis, with a knockout-score of 89% (S3 Fig). Notably in HIF1A targeted cells, HK2 protein expression was somewhat reduced, raising the possibility that HK2 could be regulated by Hif1 α (Fig 4I). We first tested the effect of HK2 and HIF1A knockout (KO) on lactate secretion compared to non-targeting guide (ntg) control cells. HK2 KO cells treated with TNF α did not induce lactate secretion relative to vehicle-treated HK2 KO cells (Fig 4J), but rather maintained basal lactate secretion observed in vehicle-treated ntg controls cells (Fig 4J). In addition to glycolysis and lactate secretion, the hexokinase-catalyzed product, glucose-6-phosphate, can be converted into glucose-1-phosphate to support the hexosamine pathway and the production of UDP-glucose (Fig 1D), the levels of which are induced by TNF α (Fig 2A). We, therefore, analyzed how HK2 contributed to TNF α -mediated induction of UDP-glucose pools and found that TNF α -induced accumulation of UDP-Glc is not affected by the absence of HK2 (Fig 4K). Together, these data suggest that HK2 is important for the full glycolytic activation induced by TNF α , but that HK2 is dispensable for basal levels of glycolysis, as well as for some other aspects of TNF α -mediated metabolic alterations, e.g., the elevation of UDP-Glc levels.

We next tested if HK2 or Hif1 α are necessary for TNF α to promote an anti-viral state. As expected, control ntg cells pretreated with TNF α in the presence of the glycolytic inhibitor 2DG are more permissive to HCMV infection compared to cells pretreated with TNF α alone (Fig 4L). However, HK2 KO and HIF1A KO cells pretreated with TNF α fully restricted HCMV initiation of infection (Fig 4L), indicating these factors are not necessary for TNF α 's anti-viral activity. Interestingly, non-TNF α treated HK2 KO and HIF1A KO cells showed an increase in HCMV plaque formation relative to the vehicle pretreated control ntg cells, suggesting that HIF1A and HK2 may play a role in restricting HCMV infection that is independent of TNF α signaling (Fig 4L).

Given that UDP-glucose is induced by TNF α and is a substrate for glycosylation reactions, we analyzed our proteomic data set to identify UDP-glucose-related enzymes that might be impacted by TNF α treatment. TNF α induced the expression of UTP-glucose-1-phosphate uridylyltransferase (UGP2), which produces UDP-Glc from Glucose-1-Phosphate [34] (Fig 4B and 4M). Further, TNF α induced the accumulation of additional enzymes involved in glycosylation, including dolichyl-phosphate beta-glucosyltransferase (ALG5), which initiates biosynthesis of lipid-linked oligosaccharides for glycosylation in the ER membrane using UDP-Glc [35] as well as alpha-1,3-mannosyl-glycoprotein 2-beta-N-acetylglucosamine transferase (MGAT1) (Fig 4M), which promotes biosynthesis of N-Glycans for glycosylation using UDP-N-Acetyl Glucosamine (UDP-GlcNAc) [36]. These data indicate that TNF α -induces the accumulation of enzymes involved in glycosyl-precursor production and glycosyltransferase activity.

Glycolytic inhibition attenuates the accumulation of intrinsic anti-viral proteins upon TNF α treatment

To get a more global picture of how glycolytic inhibition affects the TNF α -induced anti-viral state, we reexamined the proteomic data set to compare the impact of TNF α treatment in the presence and absence of 2DG (S5 Table). PCA of the total proteomics data set show that TNF α -treated samples in the presence or absence of 2DG segregated from non-TNF α treated samples largely along PC2, whereas 2DG-treated samples segregated from non-2DG treated samples along PC1 (Fig 5A). Notably, co-treatment with 2DG and TNF α blunted the TNF α -induced response as indicated by a much-reduced shift along PC2. In contrast, co-treatment with 2DG and TNF α induced a larger leftward shift along PC1 than was observed with 2DG

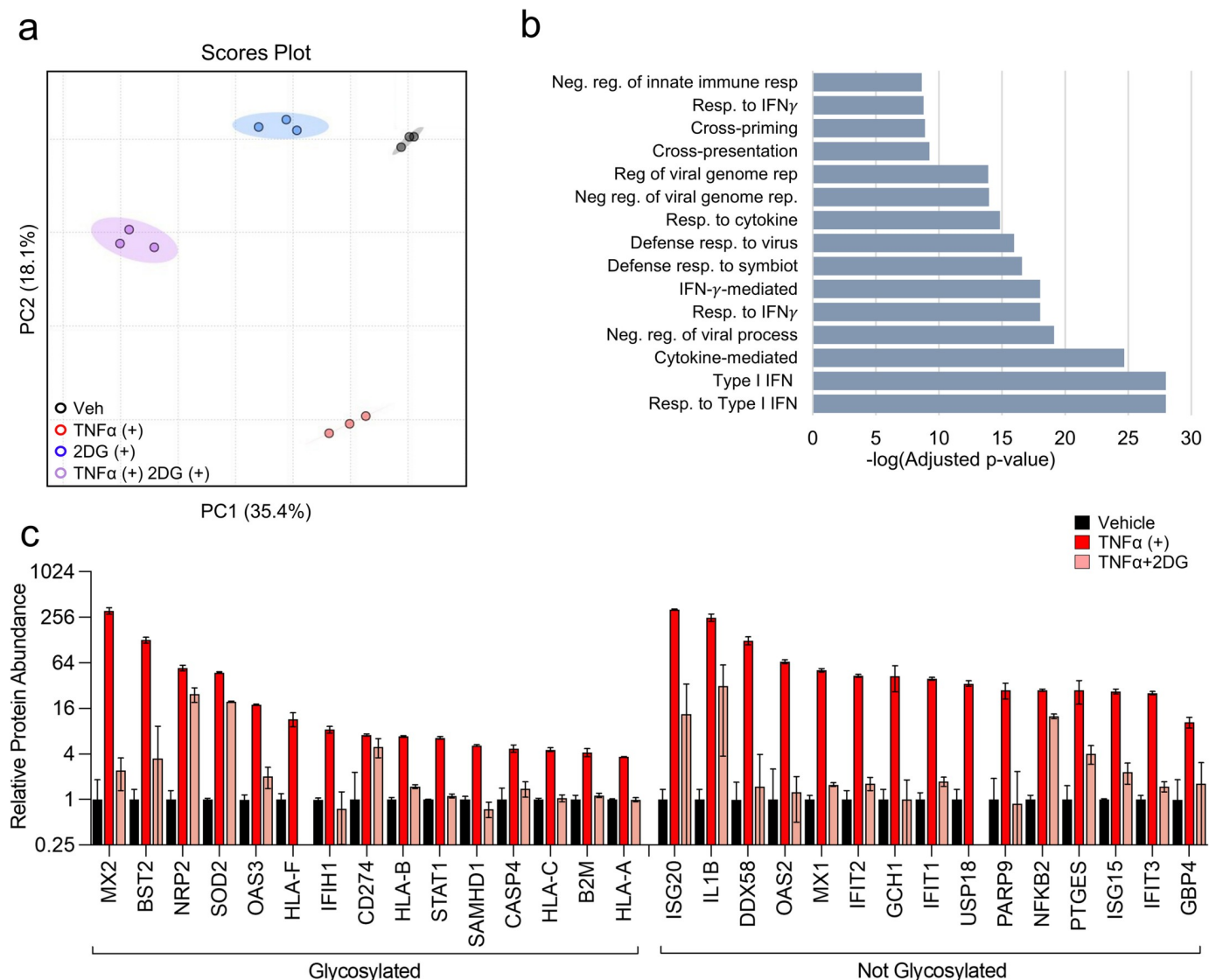


Fig 5. TNF α requires glycolysis to promote expression of intrinsic anti-viral factors and immunoregulatory proteins. (a-c) HFFs were treated with TNF α (10 ng/mL, red), 2DG (20 mM, blue), TNF α +2DG (purple) or vehicle (black) for 24 hr. Cells were harvested and analyzed by LC-MS/MS for protein abundance. **a** PCA of relative protein abundance from proteomic results. **b** Ontology analysis of TNF α -induced proteins that were significantly decreased upon co-treatment with 2DG. **c** Abundance of proteins belonging to the Response to Cytokine ontology [GO:0034097] (mean \pm SD, n = 3).

<https://doi.org/10.1371/journal.ppat.1010722.g005>

treatment alone (Fig 5A). These data suggest that 2DG treatment blunts the impact of TNF α treatment on the proteome, and further that TNF α and 2DG co-treatment accelerates the proteomic impact over 2DG alone.

To further explore the impact of 2DG treatment on TNF α -induced proteomic changes, we analyzed the proteins whose abundances were significantly depleted or induced by co-treatment with 2DG and TNF α relative to TNF α alone (S7 and S8 Tables, respectively). Gene Ontology (GO) analysis indicated that proteins significantly up-regulated in response to 2DG +TNF α co-treatment relative to TNF α treatment alone belonged to a diverse array of pathways including receptor-mediated endocytosis, the unfolded protein response, and various oxidative and metabolic stress responses (S8 Table and S4 Fig). In contrast, the pathways associated with proteins that exhibited substantially lower levels during 2DG and TNF α co-treatment relative to TNF α alone shared a common theme, they are important to the innate immune antiviral response (Fig 5B and S7 Table). These ontological pathways included responses to IFN, defense responses to viruses, and regulation of viral genome replication (Fig 5B). Approximately 33% of these proteins reduced in 2DG and TNF α co-treated cells included genes within the ontological pathway 'response to cytokine signaling', e.g., IFIs, ISGs, as well as other critical viral defense genes, e.g., MX1, OAS53, SAMHD1, and global innate regulators, e.g., STAT1 (Figs 5C and S5). Additionally, 43% of the substantially down-regulated proteins were known to be glycosylated (Figs 5C and S5). Collectively, these data indicate that restricting glycolysis during TNF α treatment prevents the accumulation of proteins involved in the anti-viral response, a substantial proportion of which are glycosylated.

TNF α treatment induces the accumulation of glycosyl precursors and glycosylation enzymes

Glucose provides the subunits necessary for protein glycosylation, which is critical for the stability of numerous glycoproteins. Given the observation that TNF α activates glycolysis, and that inhibition of glycolysis results in the decreased accumulation of several glycosylated anti-viral proteins (Fig 5C) and the apparent reduction of GLUT1 glycosylation (Fig 4F), we sought to explore the impact of TNF α on the labeling of glycosyl precursors such as UDP-Glc and UDP-N-Acetyl Glucosamine (UDP-GlcNAc). The intracellular abundance of UDP-Glc was ~3-fold higher in cells treated with TNF α for 24 hours, but UDP-GlcNAc pools remained unchanged (Fig 6A). To examine the turnover kinetics of these pools, we labeled vehicle or TNF α -treated cells with U-¹³C-glucose over time. TNF α treatment induced the accumulation rate of ¹³C-UDP-Glc and ¹³C-UDP-GlcNAc isotopologues, while increasing the rate of ¹²C isotopologue disappearance (Fig 6B and 6C), consistent with the activation of these pathways. Both UDP-Glc and UDP-GlcNAc accumulation depended on glycolysis, as inhibition with 2DG during TNF α treatment blocked the steady-state increases in UDP-Glc pools (Figs 6D and S6) and reduced the accumulation of UDP-GlcNAc (Figs 6E and S6) relative to TNF α treatment alone. Further, the U-¹³C-Glc labeling rate of the ¹³C-UDP-Glc and ¹³C-UDP-GlcNAc pools was substantially reduced upon co-treatment with TNF α treatment and 2DG (Fig 6F and 6G). These data support a model wherein TNF α treatment requires glycolysis to induce activation of UDP-sugar metabolism and support protein glycosylation of anti-viral proteins.

Glycosylation is important for the TNF α -induced anti-viral state

To dissect how various metabolic pathways including the hexosamine pathway/glycolysis contribute to TNF α 's functional ability to induce the anti-viral cell state, we pretreated cells with a variety of inhibitors that attenuate metabolic pathways adjacent to glycolysis in the presence or absence of TNF α (Fig 7A). Two inhibitors of pyrimidine biosynthesis [*N*-phosphonacetyl-L-

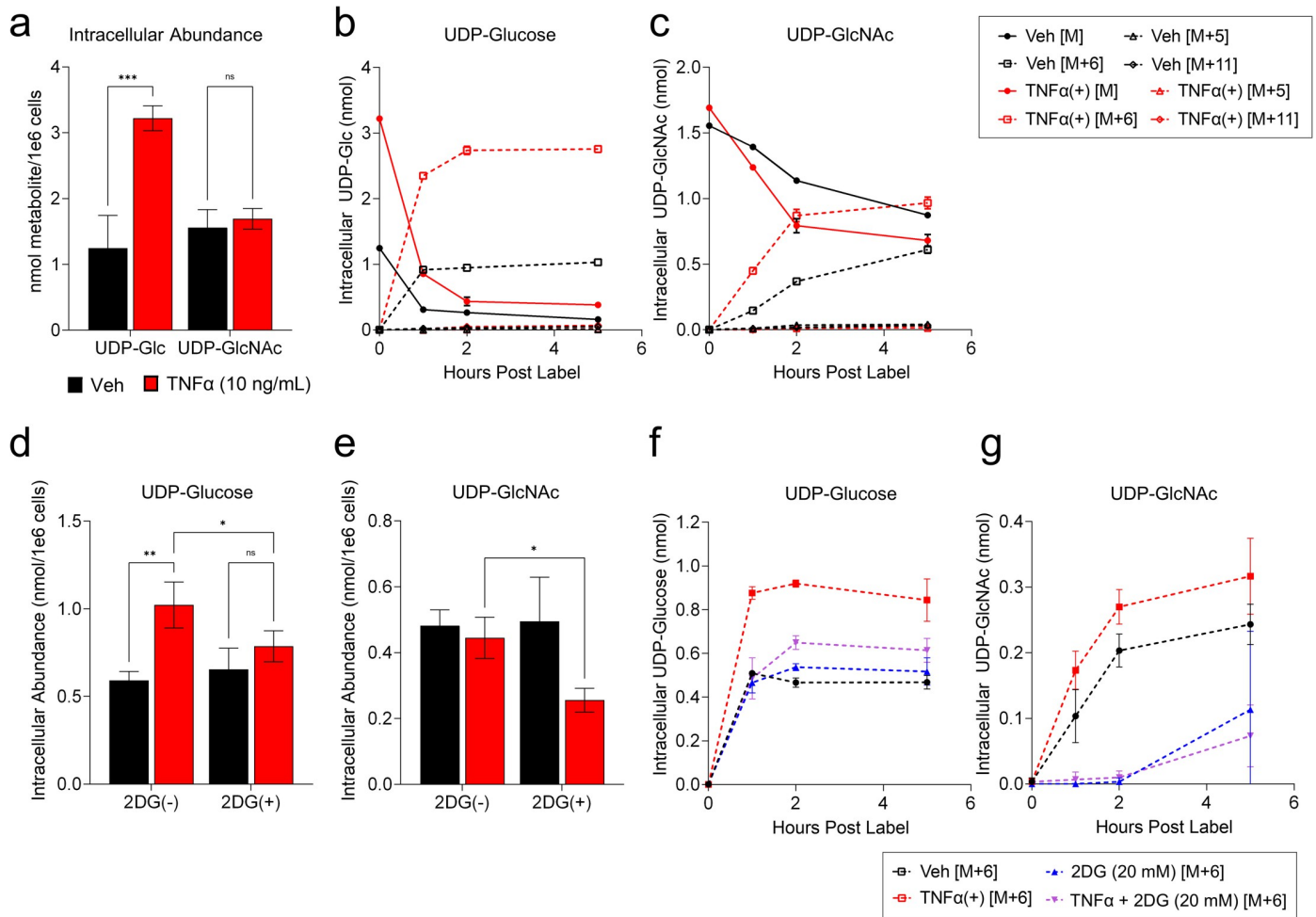


Fig 6. TNF α treatment induces glycosylation precursor turnover. a/d/e HFFs were treated as indicated for 24 hr. Metabolites extracted from cells and analyzed by LC-MS/MS for (a/d) UDP-Glucose (UDP-Glc) and (a/c) UDP-N-Acetyl Glucosamine (UDP-GlcNAc) intracellular concentrations (mean \pm SD, n = 3). b/c/f/g HFFs treated with vehicle (black), TNF α (10 ng/mL, red), 2DG (20 mM, blue) or TNF α +2DG (purple) for 19 hours in media containing unlabeled 12 C-glucose prior to media change with media containing U- 13 C-glucose, without treatments. Cellular extracts were harvested at t = 0, 1, 2 and 5 hr post-label addition. c/g UDP-Glc or d/h UDP-GlcNAc intracellular isotopologue abundances were quantified by LC-MS/MS (mean \pm SD, n = 3). Solid lines represent intracellular abundances of unlabeled 12 C metabolite species, dashed lines represent intracellular abundances of 13 C-labeled metabolite species. M refers to the 12 C unlabeled species and M+n represents detection of a 13 C-labeled species where n represents the number of additional mass units detected by mass spec. f/g represent only M+6 isotopologue abundance, refer to S6 Fig for corresponding M abundances. a/b/e/f FDR-adjusted p-values were determined using 2-way ANOVA followed by two-stage step-up method of Benjamini, Krieger and Yekutieli; ns = not significant, *p<0.05, **p<0.01, ***p<0.001.

<https://doi.org/10.1371/journal.ppat.1010722.g006>

aspartate (PALA) [37] and vidoflumidus (Vid) [38]), and two pentose phosphate pathway inhibitors [6-aminonicotinamide (6-AN) [39] and N3-pyridyl thiamine (N3-PT) [40]] failed to rescue viral replication when co-pretreated with TNF α (Fig 7A and 7B). In contrast, co-pretreatment of TNF α with BGNAc largely rescued the ability of HCMV to initiate infection. The magnitude of BGNAc rescue was indistinguishable from the rescue observed with 2DG co-pretreatment (Fig 7B). These results support a model in which protein glycosylation plays a critical role in TNF α 's ability to induce the anti-viral cell state.

Discussion

TNF α pretreatment promotes an anti-viral cell state that prevents replication of diverse viral families [10–12]. However, many questions remain about the functional requirements and

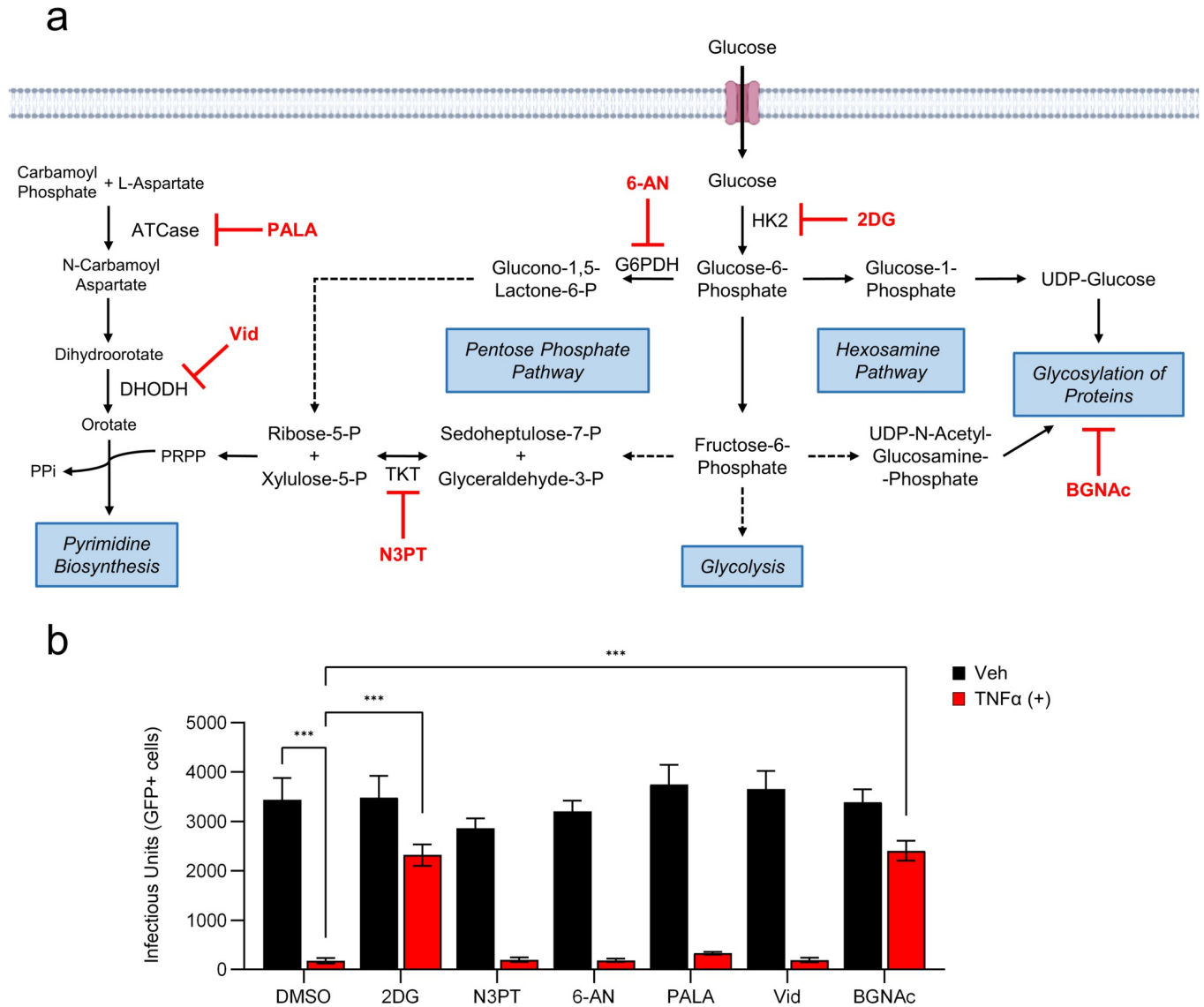


Fig 7. Inhibition of glycolysis and glycosylation restricts TNF α 's ability to induce the anti-viral state. **a** Schematic of glucose metabolism and inhibitors tested (red) during TNF α pretreatment. **b** HFFs treated with TNF α (10 ng/mL, red) or vehicle (black), in the presence or absence of 2-Deoxyglucose (2DG, 20 mM), N3-pyridyl thiamine (N3PT, 50 nM), 6-aminonicotinamide (6-AN, 200 nM), N-phosphonacetyl-L-aspartate (PALA, 150 μ M), vidliflumidus (vid, 300 nM) or Benzyl- α -GalNAc (BGNAc, 15 mM) or DMSO for 24 hr prior to a media change with fresh viral adsorption media containing glucose, but without inhibitors, and HCMV-GFP (MOI = 0.5). Infected cells were quantified by GFP expression measured at 24 hr post-infection (n \geq 6, mean \pm SD). p-values were calculated using two-way ANOVA with Tukey's multiple comparison test; *p<0.05, **p<0.01, ***p<0.001.

<https://doi.org/10.1371/journal.ppat.1010722.g007>

cellular activities responsible for limiting viral infection. In this study, we found that TNF α treatment induces significant metabolic changes, specifically activating glycolysis and inducing UDP-sugar metabolism. Further, glycolysis was necessary for the accumulation of several glycosylated anti-viral proteins. TNF α treatment also increased the accumulation of glycosyl-transferases such as ALG5 and MGAT1. Inhibiting glycolysis or glycosylation during TNF α pretreatment resulted in the loss of TNF α 's ability to attenuate viral replication. Together, these data suggest a mechanism wherein TNF α activates glycolysis and glycosylation as essential components of instituting an anti-viral state.

A key aspect of TNF α -induced glycolytic activation was the induction of HK2 expression, which was subsequently found to be important for TNF α -mediated glycolytic activation (Fig 4). Previously, TNF α has been reported to induce HK2 in a murine skeletal muscle cell line [41], but little is known about how HK2 contributes to TNF α -associated activities. HK2 is canonically thought of as the muscle-predominant hexokinase isoform, although its expression has also been found to be induced in various tumor types [42]. In tumors, it is thought to be important for cancer-cell survival through modulation of metabolic-associated stress responses [43]. While our results indicate that TNF α induces HK2 expression, which we found to be important for TNF α -induced glycolytic activation (Fig 4J), its deletion did not impact the TNF α -mediated induction of the UDP-glucose pool (Fig 4K), nor did it restore viral infection in the face of TNF α treatment (Fig 4L). This suggests that while induction of HK2 contributes to maximal TNF α -induced glycolysis, it is not essential for all aspects of TNF-induced metabolic alteration nor is it critical for TNF α -mediated inhibition of HCMV plaque formation. However, it was notable that inactivation of HK2 significantly increased HCMV-mediated plaque formation in the absence of TNF α treatment (Fig 4L), suggesting that HK2 could be playing a role in intrinsic anti-viral defense. HK2 has previously been shown to modulate mitochondrial metabolism and cell death pathways [44,45], and these aspects of HK2 metabolism could be playing important roles. Future work should explore these possibilities, as well as the possibility that HK2 induction is contributing to other aspects of TNF α -modulated innate immunity, for example, processing or presentation of viral antigens.

Hif1 α is a central regulator of glycolytic gene expression and was implicated in TNF α -mediated induction of HK2 in murine skeletal muscle cells [41], raising the possibility that Hif1 α is important for TNF α -mediated induction of glycolysis. Our data suggest that Hif1 α is dispensable for TNF α -mediated induction of lactate secretion and inhibition of HCMV replication (Fig 4J and 4L). Separately, our data show that cells lacking Hif1 α are more permissive to infection (Fig 4L), suggesting Hif1 α may play a role in limiting the initiation of infection. Consistent with this finding, Hif1 α was recently shown to attenuate HCMV replication in human fibroblasts [46]. The anti-viral phenotype associated with Hif1 α -mediated metabolic regulation is intriguing, yet the mechanisms responsible for TNF α -induced glycolysis still require elucidation.

Our data show that TNF α induces changes to several metabolic pools. Our efforts focused primarily on glycolysis, as a number of metabolites upregulated by TNF α were involved in glucose metabolism. However, the metabolite most strongly induced by TNF α treatment was kynurenine (Fig 1C). Kynurenine is a tryptophan-related metabolite that can also be considered part of the NAD⁺ biosynthetic pathway. Kynurenine accumulates in a variety of inflammatory conditions and is induced during Human Immunodeficiency Virus (HIV) infection [47,48]. Others have described pro-viral effects of kynurenine on HCMV replication [46], suggesting a potentially complex relationship with infection that requires further analysis with respect to its roles in inflammation, intrinsic immunity and during viral infection.

In addition to activation of glycolysis, we find that TNF α induces the accumulation UDP-Glucose (UDP-Glc) and stimulates the glucose-mediated labeling of both UDP-Glc and UDP-N-Acetyl-Glucosamine (UDP-GlcNAc) (Fig 6). These nucleotide sugars are molecular substrates for glycosylation reactions that are critical for a variety of cellular activities including the stability of many proteins [49,50], as well as immune cell differentiation and activation [51,52]. Our results indicate that glycolytic inhibition blocks the TNF α -mediated increases in UDP-Glc pools as well as the increases in UDP-Glc and UDP-GlcNAc labeling (Fig 6). Further, 2DG treatment blocked the TNF α -mediated accumulation of GLUT1 glycoforms without impacting the GLUT1 RNA levels or the total amount of GLUT1 protein (Fig 4). Collectively, these data suggest that TNF α induces UDP-sugar metabolism to support its anti-viral activity.

Consistent with this possibility, inhibition of O-linked glycosylation phenocopied glycolytic inhibition in that it prevented TNF α -mediated inhibition of HCMV infection, highlighting the importance of glycosylation to TNF α 's anti-viral activity (Fig 7). A number of glycosylated anti-viral effector proteins failed to accumulate upon TNF α treatment in the face of glycolytic inhibition, including MX2, BST2, OSA3 and STAT1, as did various glycosylated components of the adaptive immune response including B2M and HLA-A/B/C/F (Fig 5). These data are consistent with a model in which TNF α treatment drives UDP-sugar production to support the glycosylation and stable expression of anti-viral effector proteins.

That the expression of so many diverse anti-viral effector proteins was impacted by glycolytic inhibition in the face of TNF α treatment likely explains our findings that glycolysis is necessary to attenuate both HCMV and coronavirus replication. HCMV and the coronaviruses tested, OC43 and SARS-CoV-2, possess extremely different viral life cycles, e.g., nuclear DNA replication versus cytoplasmic RNA replication, but the anti-viral effectors downregulated by glycolytic inhibition identified in this manuscript target multiple aspects of various viral infections. These intrinsic anti-viral proteins included MX2, which can block nuclear capsid transport [53]; OAS3, whose activity can result in viral RNA degradation [54]; and BST2, which can tether viruses to membranes for degradation [55,56]. While the mechanisms through which TNF α -induced anti-viral activities rely on specific metabolic activities remain to be elucidated, collectively, our data indicate that TNF α -induced metabolic activities are broadly important for its anti-viral action.

Viruses usurp cellular metabolic resources for their replication (reviewed in [57]). As an example, HCMV induces glycolysis and respiration to support infection [30,58–63]. Similarly, SARS-CoV-2 induces glycolysis, which supports infection [64]. Whereas here, we find that glycolytic activation is important for a cytokine-induced anti-viral state. This raises the question as to whether the TNF α -induced glycolytic program is significantly different from virally-induced glycolytic programs. Potential differences could be mediated via differential macromolecular assembly of metabolic enzymes that have been found to funnel metabolic molecular flux to diverse downstream enzymes and ultimately different metabolic fates [65–67]. Further, despite similar activity increases, differential localization of metabolic enzymes can have a substantial impact on cellular physiology. As mentioned above, HK2 can be post-translationally regulated to localize to mitochondria and regulate mitochondrial metabolism and cell death pathways [44,45]. These observations in other systems suggest that substantial differences in macromolecular assembly and localization could mediate potential differences between anti-viral and pro-viral glycolytic activation. In this regard, similar mechanisms could enable anti-viral metabolic reprogramming to limit viral access to cellular metabolic resources and thereby limit various points in the viral life cycle, e.g. gene expression or genome replication. Future work in this area can begin to address these questions.

A number of non-glycosylated anti-viral proteins failed to accumulate upon TNF α treatment when glycolysis was inhibited (Fig 5), which could reflect a secondary dependence on the accumulation of a crucial glycosylated protein. STAT1, for example, is glycosylated and fails to accumulate upon TNF α treatment in the presence of glycolytic inhibition (Fig 5). Given STAT1's importance in the transcription of numerous anti-viral effectors [68], it would be predicted that its loss would deplete the expression of glycosylated and non-glycosylated anti-viral effector proteins. Potential secondary effects of losing STAT1 notwithstanding, it is still plausible that in addition to providing UDP-sugar subunits to support glycosylation, glycolysis contributes to TNF α 's anti-viral activity via other downstream metabolic activities. In this regard, many questions still remain about the molecular fate of glycolytically-derived carbon and how these pathways could contribute to TNF α 's anti-viral activity.

Our results indicate that TNF α -induced metabolic remodeling is important for its ability to promote an anti-viral state. However, many questions remain about other potential metabolic requirements for cytokine-induced intrinsic viral defense. What other cytokine-driven metabolic activities are important for limiting viral infection? What other aspects of innate immunity require specific metabolic activities, e.g., antigen processing and presentation? Is there a common anti-viral metabolic or glycosylation program induced by diverse anti-viral cytokines, e.g., TNF α , IFN γ , IFN α , etc. The answers to these questions will likely shape our understanding of an important host pathogen interaction, that is, the metabolic regulation associated with intrinsic immunity in the face of viral infection and the associated contributions to preventing viral pathogenesis.

Materials and methods

Cell culture, viruses and cell pretreatment

Telomerase-transduced Human Foreskin Fibroblasts (HFFs) and MRC5 lung fibroblasts were cultured in Dulbecco's Modified Eagle Medium (DMEM; Invitrogen #11965118) supplemented with 10% (v/v) fetal bovine serum (FBS), and 1% penicillin-streptomycin (Pen-Strep; Life Technologies #15140-122) at 37°C in a 5% (v/v) CO₂ atmosphere. VEROe6 cells (ATCC, #30-2003) were cultured in Minimum Essential Medium (MEM; Invitrogen #11090099) supplemented with 10% (v/v) fetal bovine serum (FBS), 1X GlutaMAX (Invitrogen #35050-061), and 1% Pen-Strep at 37°C in a 5% (v/v) CO₂ atmosphere. HFFs were transduced with ACE2 (HFF-ACE2) as previously described [69]. ARPE19 cells (ATCC #CRL-2302) were cultured in DMEM/F12 medium (Invitrogen, #11320082) supplemented with 10% (v/v) FBS and 1% Pen-Strep at 37°C in a 5% (v/v) CO₂ atmosphere.

The WT strain of HCMV used in experiments with MRC5s and HFFs was BADwt, a Bacterial Artificial Chromosome (BAC) clone of AD169. GFP expressing AD169, referred to as WT-GFP, was BADsubUL21.5 [70]. The clinical isolate of HCMV in this study TB40/Ewt-mCherry (TB40-mCherry) was a gift from Dr. Christine O'Connor [71] and was used in all experiments with ARPE19 cells. OC43 and SARS-CoV-2, Isolate Hong Kong/VM20001061/2020 (BEI Resources NR-52282) were cultured as previously described [69]. All experiments involving live SARS-CoV-2 were conducted in a biosafety level 3 facility at the University of Rochester using HFF-ACE2 cells. Experiments involving OC43 were performed in wild-type HFF cells, which are permissive to OC43. Viral stocks were propagated previously described [69,71] and titered using a modified Reed & Muench TCID₅₀ calculator from the Lindenbach lab [72].

For all experiments involving viral infection to determine the anti-viral effects of TNF α in the presence of different inhibitors or treatments, cells were pretreated with the indicated reagent(s) in serum-free DMEM supplemented with 1% pen/strep for 24 hours. Following this pretreatment period, treatment-containing medium was removed and replaced with virus-containing serum-free DMEM supplemented with 1% pen/strep void of any treatment so as to specifically observe the effect of pretreatment on the cell's ability to promote an anti-viral state.

Reagents and preparation of treatments

For all experiments where cells were treated with TNF α and/or inhibitors, cells were grown to confluence. Twenty-four hours prior to infection, the medium was replaced with serum-free DMEM supplemented with 1% PenStrep and appropriate compounds as indicated.

TNF α (Human) was purchased from GoldBio (#1130-01-100) and suspended in sterilized water to 1 mg/mL concentration. Aliquots of 20 μ L were stored at -80C. For experiments, TNF α was prepared in master mix solutions to 10 ng/mL concentration. 2-Deoxy-D-Glucose

(2DG) was purchased from Millipore-Sigma (#D8375-5G) and prepared to 20 mM in culture medium for experiments. 6-Aminonicotinamide (MedChem Express, Cat# HY-W01034) was suspended in DMSO to 10 mM and prepared to the indicated concentrations in culture medium. N3-pyridyl thiamine (MedChem Express, Cat# HY-16339, 5 mg) was suspended in DMSO to 8.5 mM and prepared to the indicated concentrations in culture medium. Sparfosic Acid (MedChem Express, Cat# HY-112732B) was suspended in H₂O to 10 mM and prepared to the indicated concentrations in culture medium. Vidofludimus (Cayman Chemicals, Item#18377 CAS# 717824-30-1) was suspended in DMSO to 10 mM and prepared to the indicated concentrations in culture medium. Benzyl-2-acetamido-2-deoxy- α -D-galactopyranoside (Benzyl- α -GalNAc, BGNac, MedChem Express Cat# HY-129389) suspended in H₂O to 25 mM using ultra sonication and prepared to indicated concentration in culture medium. Kifunensine (Kif, Fisher Scientific, Cat #NC1620501) was suspended in DMSO to 10 mM and prepared to the indicated concentration in cell culture medium. All treatment medium were prepared in serum-free DMEM supplemented with 1% PenStrep unless otherwise indicated. Vehicle or control treatment was serum-free DMEM supplemented with 1% PenStrep.

Plaque efficiency assay

For plaque efficiency assay, cells were grown to confluence in 12 well TC-treated Greiner plates (#82050–930) and treated as described above. Treatment medium was removed and the cell monolayer was infected with a low, known number of plaque forming units (PFUs) of AD169-GFP in 500 μ L medium overnight. Following this adsorption period, medium was removed and replaced with 2 mL of a standard agarose gel overlay prepared with 2X concentrated DMEM (Invitrogen #12100046) supplemented with 10% FBS and 1% NuSieve Agarose (Lonza, 12001–722). Plaques were allowed to develop for 10 days and the total number of plaques in each well was counted using a fluorescent microscope. For each indicated experimental condition, the total plaque count of each well was normalized to the average plaque count of the control condition.

Quantification of HCMV infectious units (GFP + cells)

HFFs were grown to confluence in 96-well TC-treated plates and then treated for 24 hours in 100 μ L indicated treatment medium. Treatment was removed and replaced with GFP-expressing HCMV viral inoculum (MOI = 0.5, 100 μ L) in serum-free DMEM, high glucose, no glutamine, no phenol red medium (Invitrogen #31053036) supplemented with 1x Glutamax and 1% Pen-Strep for 24 hours. The medium was removed and replaced with PBS containing 1:1000 diluted Hoechst fluorescent stain (Thermo Fisher #33342). HFFs were then imaged using a Cytation 5 imaging reader (BioTek). Each well was imaged using a 4X magnification objective lens and predefined DAPI channel with an excitation wavelength of 377 nm and emission wavelength of 447 nm for nuclei count, GFP channel with an excitation wavelength of 469 nm and emission wavelength of 525 nm for cells infected with AD169-GFP, or Texas Red channel with an excitation wavelength of 586 and emission wavelength of 647 for cells infected with TB40-mCherry. Gen5 software (BioTek) was used to determine cell number by gating for objects with a minimum intensity of 3000, a size greater than 5 μ m and smaller than 100 μ m.

To compare multiple models of infection as a result of pretreatments (Fig 3G), percent infection relative to vehicle was calculated individually for each model (HFF infected with AD169, MRC5 infected with AD169, ARPE19 infected with TB40e). For every model, each biological replicate from each condition was divided by the mean vehicle treated condition then multiplied by 100. Normalized values were plotted at mean \pm SD (Fig 3G).

Western blot analysis

Protein detection was performed as previously described [73]. Briefly, samples were harvested in SDS-lysis buffer (20 mM TrisHCl (VWR # 97061–794) pH 7, 5% β -Mercaptoethanol (gibco #21985–023), 2% SDS (Invitrogen #15525017), 10% Glycerol (VWR #EM-GX0185–6)), run on a 10% polyacrylamide SDS gel at 115 V for 1.5–2 hr, then transferred to 0.2 μ m nitrocellulose membrane (Bio Rad #1620112) overnight at 50 mA. Membranes were blocked with 5% milk in 1X TBS supplemented with 0.1% Tween-20 (1X TBST) for 1 hour then incubated for 2 hours or overnight in the indicated primary antibody. Membranes were rinsed 3x for 15 minutes in 1X TBST and incubated in the proper secondary antibody (Goat anti-mouse BioRad #170–6516 or Goat anti-rabbit BioRad #170–6515) for 1 hour. Membranes were rinsed 3x with 1X TBST for 15 minutes and developed using Clarity Western ECL Substrate (Bio-Rad, #1705060) and Molecular Imager Gel Doc (Bio Rad). The following antibodies were used for western blot analysis following the manufacturer's instructions: N-Protein Antibody (SinoBiological, Rabbit mAb, 40068-RP02); HK2 Hexokinase II (HK2, Cell Signaling, Rabbit mAb, C64G5) Rabbit mAb Cell signaling; Hif1 α (Novus Biologicals, Rabbit Ab, 102104–498); GAPDH (Cell Signaling, Rabbit mAb, 5174S); Glut-1 (Santa Cruz, Mouse mAb, # sc-377228); Viral proteins IE1, IE2 [74], pp28 [75], UL26 [76] (Mouse mAb).

Analysis of total glycosylated proteins

Cells were treated as previously described. Monolayer was washed 1x with cold PBS and cells scraped into cold NP-40 buffer (500 mM NaCl, 100 mM Tris pH 8.0, 1% NP-40, protease inhibitor tablet (Fisher Scientific #A32955)). Lysates were placed at 4°C on a rotator for 20 minutes and then sonicated using a sonication probe. Protein samples were processed by SDS-PAGE as indicated above and gel stained for total glycosylated protein using Pro-Q Emerald 300 glycoprotein gel and blot stain kit (Fisher Scientific #P21857) following manufacturers instructions.

Analysis of RNA

Analysis of RNA was carried out as previously described [69]. Briefly, RNA was extracted using Trizol (Invitrogen #15596026) and cDNA synthesis was completed using qScript cDNA Synthesis Kit (#95047–500). Expression of RNA was quantified by RT-qPCR for each indicated gene using the following primers: OC43: 5'-GGATTGTCGCCGACTTCTTA-3' (forward) and 5'-CACACTTCTACGCCGAAACA-3' (reverse). SARS-CoV-2: 5'-ATGAGCTTAGTCCTGTTG-3' (forward) and 5'-CTCCCTTTGTTGTGTTGT-3' (reverse). Human HK2 5'-GCC TACTTCTTCACGGAGCT-3' (forward) and 5'-ATGAGACCAGGAAACTCTCG-3' (reverse). Human Hif1 α 5'-CGTTCCTTCGATCAGTTGTC-3' (forward) and 5'-TCAGTGGTGGCAGTGGTAGT-3' (reverse). Human Glut1: 5'-GCCTTCTTTGAAGTGGGTCC-3' (forward) and 5'-AGTTGGAGAAGCCTGCAACG-3' (reverse). Gene expression was normalized to Human GAPDH: 5'-CATGTTTCGTCATGGGTGTGAACCA-3' (forward) and 5'-ATGGCATGGACTGTGGTCATGAGT-3'.

CRISPR knockout

CRISPR knockouts (KO) were performed with the Neon Transfection System 10 μ L kit (ThermoFisher #MPK1025). HFFs were grown to 70% confluence and trypsinized using TrypLE Express (Invitrogen #12605010). HFFs were collected via centrifugation at 600 RPM for 5 minutes and resuspended to a concentration of 1.1×10^7 in resuspension buffer R (ThermoFisher #MPK1025). In a separate tube, 60 pmol sgRNA was combined with 20 pmol Cas9 protein

(Synthego) in a volume of 3 μ L and incubated at room temperature for 15 minutes. To the prepared sgRNA:Cas9 mixture, 9 μ L cell solution (2×10^5 HFFs) was added and gently pipetted up and down to mix. A 10 μ L Neon pipette tip was used to extract 10 μ L of the cell/sgRNA/Cas9 solution which was then electroporated using the Neon Transfection System (voltage: 1650 V, width: 10 ms, pulses: 3) and transferred to a prepared 6-well dish (Greiner #82050–842) containing growth medium. This process was repeated with the same pipette tip and sgRNA/Cas9 solution and transferred to the same dish for 2 transfections per guide into a single well.

Guide RNAs were ordered from Synthego—Negative Control Scrambled sgRNA (modified) #1: GCACUACCAGAGCUAACUCA, HK2 (Gene Knockout Kit v2): sg1-CAUGCACGGCACCGGGGACG sg2-UCCGUGUUCGAAUGGGAAG sg3-UCCAGAGAAAGGGGACUUCU, HIF1A (Gene Knockout Kit v2): sg1- AGGAAAGUCUUGCUAUCUAA sg2- UUCACAAAUCAGCACCAAGC sg3- ACACAGGUAUUGCACUGCAC.

Synthego ICE score [77]

Knockout confirmation of HIF1A using Synthego's Inference of CRISPR Edits (ICE). Genomic DNA was extracted from a 10 cm dish of sub-confluent HFFs transfected with HIF1A sgRNA/Cas9 (described above) or non-target guide control (ntg) sgRNA/Cas9 ribonucleoprotein complex using Lucigen quick extract DNA kit (item # QE09050). HIF1A gene locus surrounding the sgRNA target site was amplified from HIF1A edited DNA extract sample and ntg control DNA extract sample with HIF1A primer set 1 (sequences below) using touchdown PCR method. The resulting DNA fragment was PCR purified using Qiagen QIAquick PCR purification kit (item # 28104) and used as the DNA template in a second PCR method using HIF1A primer set 2 (Sequences below). The resulting DNA fragment was purified as described above and submitted to Genewiz for Sanger Sequencing using Hif1 α primer set 3 (sequences below). Sequencing data for HIF1A edited and ntg control samples were uploaded to ice.synthego.com for analysis [77]. Primer sequences: HIF1A Set 1: F-GGGAAGGTTTACAGTTCCATGG; R-GTCTTGCTCTGTCATCCAGG. HIF1A Set 2: F-TCCAGGCTTAATCAGTTGGC; R-CTCAGCTCACCACAACATCC. HIF1A Set 3: F- GCAGCCTAGACTTTA TACGAGG; R-ATCTCCTGACCTCAGATGATCC.

Glucose consumption

HFFs were grown to confluence in a 6-well TC-treated plate (Greiner #82050–842) and treated with 1 mL indicated treatment master mix for 24 hours. The medium was harvested from each well and glucose concentration for each medium sample was quantified using the HemoCue Glucose 201 System (HemoCue).

A standard curve was prepared using virgin medium where the highest dilution was 225 mg/dL glucose. This standard was serially diluted in PBS 1:2 five times for the remaining standards. To detect glucose, 8 μ L each standard was loaded into a HemoCue glucose microcuvette (Hemocue #10842–830) and inserted into the glucose meter; mg/dL glucose detected was recorded and plot against the known concentration of glucose in the standards. Samples were diluted 1:4 in PBS and loaded into microcuvettes as described for standards.

To calculate glucose consumption, mg/dL glucose was determined for each sample using the standard curve and then multiplied by its dilution. The amount of glucose detected in each sample was subtracted from the amount of glucose in t0 medium to quantify the total nmol glucose consumed over 24 hr. The total amount of glucose consumed (nmol/hrx1e6 cells) was calculated by dividing the calculated nmol glucose consumed for each sample by 24 hr and the average HFF cell count in a 6-well dish (3.1×10^5 cells).

Lactate secretion

HFFs were grown to confluence in a 12-well TC-treated plate and treated with 500 μL indicated treatment master mix for 24 hours. The medium was harvested from each well and stored at -80°C . To measure lactate in the medium, a standard curve was prepared using a 16 mM lactate standard as the most concentrated standard and serially diluting this most concentrated standard 1:2 8x. Medium samples were diluted 1:64 in PBS. Samples and standards were loaded onto the same MS run and the resulting MS intensity data of the standards was used to generate a standard curve. Standards that began to plateau or fell below the limit of detection (3x the value of the average blank) were discarded from the standard curve. Sample MS intensity values that did not fall within the standard curve were not quantified.

Lactate secretion for each sample was calculated by converting the MS intensity value to mM lactate using the standard curve and multiplying by the dilution factor (1:64) to yield lactate concentration (nmol/ μL). Total nmol for each sample was calculated by multiplying the lactate concentration by the total sample volume (500 μL). Lactate secretion (nmol/hr* $1\text{e}6$ cells) was calculated by dividing the total nmol lactate secreted for each sample by 24 hr and the average HFF cell count in a 12 well plate ($1.2\text{e}5$ cells).

Steady state metabolomics analysis

For steady state metabolomics, HFFs were grown to confluence in 10 cm TC-treated dishes (Greiner #82050–916) and placed in serum-free medium supplemented with 10 mM HEPES for 24 hours. HFFs were treated with 7 mL treatment medium supplemented with 10 mM HEPES for 24 hours. The medium was aspirated and metabolites were extracted from cells immediately by adding 3 mL cold 80% methanol (-80°C). Extract was centrifuged at 3,000 RPM and supernatant containing metabolites was decanted into a fresh 50 mL conical on dry ice. Residual metabolites were extracted from the cell pellet with 3x washes of 500 μL 80% cold methanol followed by centrifugation at 3,000 RPM. Supernatants were pooled in the appropriate 50 mL conical and the methanol was evaporated under a gentle stream of nitrogen for 6–8 hours. Samples were suspended in 200 μL 80% cold methanol and analyzed by LC-MS/MS as previously described [78] along 8x standards serially diluted 1:2 where the most concentrated standard contained: Glucose-6-phosphate (25 μM), Glucose-1-Phosphate (25 μM), Fructose-6-Phosphate (2.5 μM), Fructose-1,6-Bisphosphate (20 μM), UDP-Glucose (50 μM), N-Acetyl Glucosamine-6-Phosphate (20 μM), UDP-N-Acetyl Glucosamine (40 μM) and N-Acetyl Glucosamine-1-Phosphate (20 μM). Absolute abundances of UDP-Glc and UDP-GlcNAc (Fig 6A/6D/6E) were calculated by converting MS intensity to nmol/ μL UDP-Glc or UDP-GlcNAc using the appropriate standard curve. Total metabolite (nmol) in each sample was determined by multiplying total sample volume (200 μL) by the calculated metabolite concentration (nmol/ μL). Total intracellular metabolite abundance (nmol/ $1\text{e}6$ cells) was determined by dividing the nmol metabolite by the average HFF cell count in a 10 cm dish ($1.7\text{e}6$ cells).

For metabolomics data analysis, LC-MS/MS intensity values were imported to Metaboanalyst 5.0 [79]. R-history for metaboanalyst can be found in [S1 Data](#). The data were mean-centered and divided by the standard deviation (SD) of each variable. For principal component analysis, each dot represents metabolomics data of one biologically independent sample. Shaded ellipses represent 95% confidence intervals. PC1 and PC2 refer to the amount of total variation observed between samples that can be attributed to segregation along that principal component. Hierarchical clustering maps follow Euclidian distance and Ward cluster algorithm. Metabolite values are depicted as Z-scores from min (blue) to max (red). Metabolites determined to be significantly different between TNF α and vehicle treatments (Fig 1C) were determined in Metaboanalyst. Log₂ fold change (FC) values and FDR-adjusted p-values were

calculated using Metaboanalyst. The direction of comparison was TNF α +/Vehicle. FC threshold of 1.5 and FDR-adjusted p-value threshold of 0.05 were applied to yield 12 metabolites significantly altered as a result of TNF α treatment.

Metabolic tracer analysis

HFFs were grown to confluence in 10 cm dishes in growth medium. Medium was replaced with serum-free medium containing 10 mM HEPES for 24 hours. Cells were then treated with 7 mL indicated treatment medium made using glucose-free DMEM (Invotrogen #11966025) supplemented with 10 mM HEPES and ^{12}C -Glucose (4.5 g/L) for 19 hours. At 19 hours, medium was replaced with 7 mL glucose-free DMEM supplemented with 10 mM HEPES containing U- ^{13}C -Glucose (Cambridge Isotopes #CLM-1396-1) (4.5 g/mL). Metabolites were extracted from cells as described above at 19 hours post treatment ($t = 0$ hours post label), 20 hours post treatment ($t = 1$ hours post label), 21 hours post treatment ($t = 2$ hours post label) and 25 hours post treatment ($t = 5$ hours post label). Samples were prepared and analyzed by LC-MS/MS as described above [78]. To analyze the intracellular abundance of isotopologues as represented in Fig 6B/6D/6F/6G, each isotopologue species was divided by the sum of all isotopologues detected and multiplied by the intracellular abundance of UDP-Glc or UDP-GlcNAc determined in Fig 6A/6D/6E.

Proteomics experiment and data analysis

Cells were grown to confluence in 10 cm dishes (VWR, #82050–916) and placed in serum-free medium for 24 hours. Cells were treated in 7 mL indicated treatment medium at t_0 . At 24 hr post treatment, the monolayer was washed 3x with cold PBS. All subsequent steps were performed on ice and with chilled 4C PBS. Cells were scraped in 3 mL PBS and transferred to 15 mL conical tubes. Each dish was washed with an additional 3 mL of PBS and combined with its respective cell suspension. For each sample, cells were pelleted via centrifugation at 3,000 RPM for 5 minutes. Supernatant was discarded and the pellet was washed with 500 μL cold PBS and pelleted again at 3,000 RPM for 5 minutes. Supernatant was removed and samples were brought to the Mass Spectrometry Resource Laboratory (MSRL) at University of Rochester Medical Center. Protein extraction and S-trap Digest was performed by the MSRL. Samples were run on Oribtrap Fusion Lumos and analyzed using Data-Independent Acquisition (DIA) to yield relative protein abundance for 3,780 proteins, data shown in S5 Table. Data uploaded to MetaboAnalyst 5.0, mean-centered and divided by the standard deviation (SD) of each variable. For principal component analysis (Fig 5A) each dot represents proteomics data of one biologically independent sample. Shaded ellipses represent 95% confidence intervals. PC1 and PC2 refer to the amount of total variation observed between samples that can be attributed to segregation along that principal component.

To observe the differences in abundance of metabolic enzymes between vehicle and TNF α treated cells, a list of genes involved in metabolism was retrieved from the UniProt Database on August 31st, 2021 to yield 4,432 human genes involved in metabolism (S6 Table). This list of genes was scanned against our proteomics data set of 3,780 proteins using a custom code in Python v 3.7/PyCharm Community 12.1. The resulting list of intersecting genes (562 genes) were uploaded to MetaboAnalyst 5.0. R-history for metaboanalyst can be found in S1 Data. Data were mean-centered and divided by the standard deviation (SD) of each variable. For principal component analysis (S1 Fig) each dot represents proteomics data of one biologically independent sample. Shaded ellipses represent 95% confidence intervals. PC1 and PC2 refer to the amount of total variation observed between samples that can be attributed to segregation along that principal component. Hierarchical clustering maps (Fig 4A) follow Euclidian

distance and Ward cluster algorithm. Values are depicted as Z-scores from min (blue) to max (red). Proteins determined to be significantly more or less abundance as a result of TNF α -treatment relative to vehicle were determined in Metaboanalyst. Log₂ fold change (FC) values and FDR-adjusted p-values were calculated using Metaboanalyst (S6 Table). The direction of comparison was TNF α +Vehicle. FC threshold of 1.5 and FDR-adjusted p-value threshold of 0.05 were applied to yield 40 proteins significantly altered as a result of TNF α treatment.

For the analysis of a specific protein of interest, normalized protein abundance was calculated by dividing each sample relative protein abundance by the average of the vehicle-treated relative protein abundance (Fig 4C/4G/4M). Statistics were performed in GraphPad Prism v9.1.0.

To generate a list of proteins more abundant in TNF α treatment compared to TNF α +2DG co-treatment, statistical parameters were applied to the data [Log₂ Fold Change (TNF α +2DG/TNF α) < -0.6, p-value < 0.05] (S7 Table, 239 proteins). The resulting list of proteins which were uploaded to Gene Ontology (GO) Analysis to identify the biological process most impacted, represented by FDR-values (Fig 5B). The list of proteins more abundant in TNF α treatment compared to TNF α +2DG co-treatment was also scanned against the GO-term [GO:0034097] "Involved in Cytokine Signaling" (54 proteins). These genes were scanned against databases of known glycosylated proteins [80,81] using a customized R-script to identify glycosylated proteins within this subset of proteins more abundant in TNF α treatment that are depleted during TNF α +2DG co-treatment (30 proteins glycosylated, 24 proteins not glycosylated). Missing values were replaced with the minimum detected MS intensity detected by that sample (S7 Table, yellow highlighted cells). Relative protein abundance values for each protein was determined by dividing the sample normalized protein abundance by the average relative protein abundance of vehicle-treated for that protein. The top 15 proteins most strongly induced by TNF α treatment, either glycosylated or not glycosylated, were graphed (Fig 5C).

Similarly, a list of proteins more abundant in TNF α +2DG co-treatment compared to TNF α treatment was generated by applying statistical parameters to the original proteomics list of 3,780 proteins [Log₂ Fold Change (TNF α +2DG/TNF α) < 0.6, p-value < 0.05] (S8 Table, 120 proteins). The resulting list of proteins was uploaded to Gene Ontology (GO) Analysis to identify the biological processes most impacted, represented by FDR-values (S4 Fig)

Statistics

All statistical analysis were carried out using GraphPad Prism v9.1.0 unless otherwise indicated. MetaboAnalyst 5.0 was used to perform PCA analysis and hierarchical clustering from raw LC-MS/MS intensity data mean-centered and divided by the standard deviation (SD) of each variable. R-history for metaboanalyst can be found in S1 Data.

Supporting information

S1 Fig. HFFs treated with vehicle (black) or TNF α (10 ng/mL, red) for 24 hr. Cells were harvested for proteomics analysis (S5 Table). PCA of a subset of proteins from proteomics analysis involved in metabolism; analysis described in materials and methods (S6 Table). Data shared with Fig 4A.

(TIF)

S2 Fig. Protein lysates of HFFs treated with vehicle, TNF α (10 ng/mL), 2DG (20 mM), BGNac (15 mM) or Kif (5 μ M) for 24 hours and assayed for total glycosylated proteins using Pro-Q Emerald 300 glycoprotein gel and blot stain kit.

(TIF)

S3 Fig. Knockout confirmation of Hif1 α using Synthego's Inference of CRISPR Edits (ICE) tool. HFFs treated with CRISPR Cas9-RNP containing guides for HIF1A or a non-target guide (ntg) to generate knockout (KO) cell lines. HIF1A and ntg targeted cells harvested for genomic DNA and HIF1A gene locus amplified with sequencing primers. Sanger sequencing results uploaded to Synthego's ICE tool. **a** Alignment plot, left, showing control (orange) and edited (green) sequences. Vertical dotted lines indicate guide sequences in relation to Sanger sequence coordinates. Indel plot, right, showing the predicted range of insertions and deletions in the edited gene locus. **b** Trace files of HIF1A (edited sample) and ntg (control sample) targeted cells spanning the cut site of HIF1A gene locus targeted by sgRNAs. Guide sequences underlined by black solid line in the control trace, PAM sequences denoted by dotted red underline and vertical dotted lines indicate expected cut site. **c** Table from ICE analysis displaying ICE and KO score as well as sgRNA sequences towards HIF1A.

(TIF)

S4 Fig. HFFs treated with vehicle and TNF α (10 ng/mL) in the presence and absence of 2DG (20 mM) for 24 hr. Cells harvested and analyzed for protein abundance (S5 Table). Ontology analysis of TNF α -induced proteins that were significantly more abundant upon co-treatment with 2DG. Bar graph represents the FDR-values from the top 15 GO-terms (S8 Table).

(TIF)

S5 Fig. Proteomics analysis workflow. HFFs treated with vehicle and TNF α (10 ng/mL) in the presence and absence of 2DG (20 mM) 24 hr. Cells harvested and analyzed for protein abundance (S5 Table). Statistical parameters applied to proteomics data, described in materials and methods, to generate a list of proteins significantly induced by TNF α treatment but depleted in cells co-treated with TNF α and 2DG. Protein list submitted for Gene Ontology (GO) analysis (Fig 6B) and scanned against databases of known glycosylated proteins (described in materials and methods) or 'Response to Cytokine Signaling' [GO:0034097] (S7 Table). Venn Diagram represents overlap of proteins involved in cytokine signaling (yellow) and glycosylated (blue).

(TIF)

S6 Fig. HFFs treated with vehicle (black), TNF α (10 ng/mL, red), 2DG (20 mM, blue) or TNF α +2DG (purple) for 19 hours in media containing unlabeled ^{12}C -glucose prior to media change with media containing U- ^{13}C -glucose, but without treatments. Cellular extracts were harvested at t = 0, 1, 2 and 5 hr post-label addition. UDP-Glc or UDP-GlcNAc intracellular isotopologue abundances were quantified by LC-MS/MS (mean \pm SD, n = 3). Solid lines represent intracellular abundances of unlabeled ^{12}C metabolite species, dashed lines represent intracellular abundances of ^{13}C -labeled metabolite species. M refers to the ^{12}C unlabeled species and M+n represents detection of a ^{13}C -labeled species where n represents the number of additional mass units detected by mass spec.

(TIF)

S1 Table. Cells treated with TNF α (10 ng/mL) or vehicle for 24 hours (n = 3). Metabolites extracted and analyzed by LC-MS/MS. Table represents the LC-MS/MS intensity raw values. Data uploaded to Metaboanalyst v5.0 for analysis as described in materials and methods (Fig 1A and 1B).

(XLSX)

S2 Table. Table represents statistical analysis of LC-MS/MS intensity values from S1 Table analyzed by MetaboAnalyst v5.0. Comparison is [TNF α /Vehicle], metabolites highlighted in

yellow are those with a 1.5 fold change (FC) cutoff and FDR < 0.05 (Fig 1C).
(XLSX)

S3 Table. Cells treated with TNF α (10 ng/mL) or vehicle. Metabolites harvested at t0, 4, 12 and 24 hours post treatment (hpt, n = 3). Table represents LC-MS/MS intensity raw values (rows 1–28). Data from t = 4, 12 & 24 hpt median-normalized (Rows 32–59) and analyzed using students ttest as described in materials & methods (Columns AA-AC). Data represented in Fig 2A.
(XLSX)

S4 Table. Cells treated with TNF α (10 ng/mL), 2-Deoxy-D-Glucose (20 mM) or vehicle as indicated for 24 hours (n = 4). Metabolites extracted and analyzed by LC-MS/MS. Table represents the LC-MS/MS intensity raw values. Data uploaded to Metaboanalyst v5.0 for analysis as described in materials and methods (Fig 3A and 3B).
(XLSX)

S5 Table. Cells treated with TNF α (10 ng/mL), 2-Deoxy-D-Glucose (20 mM) or vehicle as indicated for 24 hours (n = 4). Protein harvested from cells analyzed by LC-MS/MS. Data uploaded to Metaboanalyst v5.0 for analysis as described in materials and methods (Fig 5A).
(XLSX)

S6 Table. Intersection of proteins from proteomics experiment (S5 Table, Veh & TNF α groups) and entries from Uniprot database involved in ‘metabolism’ (Column A). Table represents the subset of proteins detected in this study involved in metabolism and their relative abundance (562 proteins total, Columns C-K). Data analyzed using Metaboanalyst v5.0 as described in materials and methods, comparison is [TNF α /Veh]. Cells highlighted in yellow are proteins more abundant in TNF α -treated cells relative to vehicle with a 1.5 FC cutoff and FDR < 0.05 (Columns M-O). Data is shared with Fig 4A and 4C.
(XLSX)

S7 Table. Analysis of proteomics data (S5 Table) to identify proteins in the TNF α +2DG treatment group that were significantly more or significantly less abundant relative to TNF α treatment group. See Materials and methods for details. Orange: subset of proteins from S5 Table significantly induced by TNF α treatment relative to vehicle, and depleted during TNF α treatment in the presence of 2DG relative to TNF α treatment alone. Blue: Gene Ontology analysis output of the 239 proteins significantly induced by TNF α treatment relative to vehicle, and depleted during TNF α treatment in the presence of 2DG relative to TNF α treatment alone. Bold ontology terms are represented in Fig 5B. Yellow = Limit of detection (LOD) data imputation values (see materials & methods) Pale yellow: proteins significantly induced by TNF α treatment relative to vehicle, and depleted during TNF α treatment in the presence of 2DG relative to TNF α . Pale green: proteins significantly induced by TNF α treatment relative to vehicle, and depleted during TNF α treatment in the presence of 2DG relative to TNF α treatment alone that are involved in response to cytokine and are known to be glycosylated (Fig 5B and 5C).
(XLSX)

S8 Table. Subset of proteins from S5 Table significantly more abundant in cells treated with TNF α treatment in the presence of 2DG relative to TNF α treatment (Columns A-C). Output of Gene Ontology analysis of column A (Columns F-K). Data represented in S4 Fig.
(XLSX)

S1 Data. R history codes for Metaboanalyst v5.0 analyses.
(DOCX)

Author Contributions

Conceptualization: Jessica Ciesla, Isreal Moreno, Jr., Joshua Munger.

Formal analysis: Jessica Ciesla, Isreal Moreno, Jr., Joshua Munger.

Funding acquisition: Joshua Munger.

Investigation: Jessica Ciesla, Isreal Moreno, Jr.

Methodology: Jessica Ciesla, Isreal Moreno, Jr.

Supervision: Joshua Munger.

Writing – original draft: Jessica Ciesla, Joshua Munger.

Writing – review & editing: Jessica Ciesla, Isreal Moreno, Jr., Joshua Munger.

References

1. Ahmad FB, Cisewski JA, Minino A, Anderson RN. Provisional Mortality Data—United States, 2020. *MMWR Morb Mortal Wkly Rep.* 2021; 70(14):519–22. Epub 20210409. <https://doi.org/10.15585/mmwr.mm7014e1> PMID: 33830988; PubMed Central PMCID: PMC8030985.
2. Gerna G, Baldanti F, Revello MG. Pathogenesis of human cytomegalovirus infection and cellular targets. *Hum Immunol.* 2004; 65(5):381–6. <https://doi.org/10.1016/j.humimm.2004.02.009> PMID: 15172435.
3. Pass RF. Cytomegalovirus. In: Knipe DM, Howley PM, editors. *Fields' Virology*. 4th ed. New York: Lippincott-Williams and Wilkins; 2001. p. 2675–705.
4. CDC. Congenital CMV and Hearing Loss: Center for Disease Control; 2020 [updated April 28th, 2020; cited 2021 October 3rd 2021]. Available from: <https://www.cdc.gov/cmV/hearing-loss.html>.
5. Medzhitov R. Toll-like receptors and innate immunity. *Nat Rev Immunol.* 2001; 1(2):135–45. <https://doi.org/10.1038/35100529> PMID: 11905821.
6. Channappanavar R, Perlman S. Pathogenic human coronavirus infections: causes and consequences of cytokine storm and immunopathology. *Semin Immunopathol.* 2017; 39(5):529–39. Epub 2017/05/04. <https://doi.org/10.1007/s00281-017-0629-x> PMID: 28466096; PubMed Central PMCID: PMC7079893.
7. Watkins LR, Maier SF, Goehler LE. Immune activation: the role of pro-inflammatory cytokines in inflammation, illness responses and pathological pain states. *Pain.* 1995; 63(3):289–302. [https://doi.org/10.1016/0304-3959\(95\)00186-7](https://doi.org/10.1016/0304-3959(95)00186-7) PMID: 8719529
8. Schoggins JW. Interferon-stimulated genes: roles in viral pathogenesis. *Curr Opin Virol.* 2014; 6:40–6. Epub 20140405. <https://doi.org/10.1016/j.coviro.2014.03.006> PMID: 24713352; PubMed Central PMCID: PMC4077717.
9. Schneider WM, Chevillotte MD, Rice CM. Interferon-stimulated genes: a complex web of host defenses. *Annu Rev Immunol.* 2014; 32:513–45. Epub 20140206. <https://doi.org/10.1146/annurev-immunol-032713-120231> PMID: 24555472; PubMed Central PMCID: PMC4313732.
10. Mestan J, Digel W, Mittnacht S, Hillen H, Blohm D, Moller A, et al. Antiviral effects of recombinant tumour necrosis factor in vitro. *Nature.* 1986; 323(6091):816–9. Epub 1986/10/05. <https://doi.org/10.1038/323816a0> PMID: 3022155.
11. Cheeran MC, Hu S, Gekker G, Lokensgard JR. Decreased cytomegalovirus expression following proinflammatory cytokine treatment of primary human astrocytes. *J Immunol.* 2000; 164(2):926–33. Epub 2000/01/07. <https://doi.org/10.4049/jimmunol.164.2.926> PMID: 10623841.
12. Laidlaw SM, Marukian S, Gilmore RH, Cashman SB, Nechyporuk-Zloy V, Rice CM, et al. Tumor Necrosis Factor Inhibits Spread of Hepatitis C Virus Among Liver Cells, Independent From Interferons. *Gastroenterology.* 2017; 153(2):566–78 e5. Epub 2017/05/01. <https://doi.org/10.1053/j.gastro.2017.04.021> PMID: 28456632; PubMed Central PMCID: PMC5627365.
13. Rawlings JS, Rosler KM, Harrison DA. The JAK/STAT signaling pathway. *J Cell Sci.* 2004; 117(Pt 8):1281–3. <https://doi.org/10.1242/jcs.00963> PMID: 15020666.

14. Ghosh S, May MJ, Kopp EB. NF-kappa B and Rel proteins: evolutionarily conserved mediators of immune responses. *Annu Rev Immunol.* 1998; 16:225–60. <https://doi.org/10.1146/annurev.immunol.16.1.225> PMID: 9597130.
15. Yan N, Chen ZJ. Intrinsic antiviral immunity. *Nat Immunol.* 2012; 13(3):214–22. Epub 20120216. <https://doi.org/10.1038/ni.2229> PMID: 22344284; PubMed Central PMCID: PMC3549670.
16. Doughty CA, Bleiman BF, Wagner DJ, Dufort FJ, Mataraza JM, Roberts MF, et al. Antigen receptor-mediated changes in glucose metabolism in B lymphocytes: role of phosphatidylinositol 3-kinase signaling in the glycolytic control of growth. *Blood.* 2006; 107(11):4458–65. Epub 2006/02/02. <https://doi.org/10.1182/blood-2005-12-4788> PMID: 16449529; PubMed Central PMCID: PMC1895797.
17. Dufort FJ, Bleiman BF, Gumina MR, Blair D, Wagner DJ, Roberts MF, et al. Cutting edge: IL-4-mediated protection of primary B lymphocytes from apoptosis via Stat6-dependent regulation of glycolytic metabolism. *J Immunol.* 2007; 179(8):4953–7. Epub 2007/10/04. <https://doi.org/10.4049/jimmunol.179.8.4953> PMID: 17911579.
18. Pearce EL, Walsh MC, Cejas PJ, Harms GM, Shen H, Wang LS, et al. Enhancing CD8 T-cell memory by modulating fatty acid metabolism. *Nature.* 2009; 460(7251):103–7. Epub 2009/06/06. <https://doi.org/10.1038/nature08097> PMID: 19494812; PubMed Central PMCID: PMC2803086.
19. Sena LA, Li S, Jairaman A, Prakriya M, Ezponda T, Hildeman DA, et al. Mitochondria are required for antigen-specific T cell activation through reactive oxygen species signaling. *Immunity.* 2013; 38(2):225–36. Epub 2013/02/19. <https://doi.org/10.1016/j.immuni.2012.10.020> PMID: 23415911; PubMed Central PMCID: PMC3582741.
20. Cramer T, Yamanishi Y, Clausen BE, Förster I, Pawlinski R, Mackman N, et al. HIF-1alpha is essential for myeloid cell-mediated inflammation. *Cell.* 2003; 112(5):645–57. Epub 2003/03/12. [https://doi.org/10.1016/s0092-8674\(03\)00154-5](https://doi.org/10.1016/s0092-8674(03)00154-5) PMID: 12628185; PubMed Central PMCID: PMC4480774.
21. Furukawa S, Saito H, Inoue T, Matsuda T, Fukatsu K, Han I, et al. Supplemental glutamine augments phagocytosis and reactive oxygen intermediate production by neutrophils and monocytes from postoperative patients in vitro. *Nutrition (Burbank, Los Angeles County, Calif.)* 2000; 16(5):323–9. Epub 2000/05/04. [https://doi.org/10.1016/s0899-9007\(00\)00228-8](https://doi.org/10.1016/s0899-9007(00)00228-8) PMID: 10793298.
22. Haschemi A, Kosma P, Gille L, Evans CR, Burant CF, Starkl P, et al. The sedoheptulose kinase CARKL directs macrophage polarization through control of glucose metabolism. *Cell metabolism.* 2012; 15(6):813–26. Epub 2012/06/12. <https://doi.org/10.1016/j.cmet.2012.04.023> PMID: 22682222; PubMed Central PMCID: PMC3370649.
23. Odegaard JI, Chawla A. Alternative macrophage activation and metabolism. *Annual review of pathology.* 2011; 6:275–97. Epub 2010/11/03. <https://doi.org/10.1146/annurev-pathol-011110-130138> PMID: 21034223; PubMed Central PMCID: PMC3381938.
24. Vats D, Mukundan L, Odegaard JI, Zhang L, Smith KL, Morel CR, et al. Oxidative metabolism and PGC-1beta attenuate macrophage-mediated inflammation. *Cell metabolism.* 2006; 4(1):13–24. Epub 2006/07/04. <https://doi.org/10.1016/j.cmet.2006.05.011> PMID: 16814729; PubMed Central PMCID: PMC1904486.
25. Nishizuka Y, Hayaishi O. Studies on the Biosynthesis of Nicotinamide Adenine Dinucleotide. *Journal of Biological Chemistry.* 1963; 238(10):3369–77. [https://doi.org/10.1016/s0021-9258\(18\)48675-9](https://doi.org/10.1016/s0021-9258(18)48675-9) PMID: 14085389
26. Bender DA, Olufunwa R. Utilization of tryptophan, nicotinamide and nicotinic acid as precursors for nicotinamide nucleotide synthesis in isolated rat liver cells. *Br J Nutr.* 1988; 59(2):279–87. <https://doi.org/10.1079/bjn19880035> PMID: 2965917.
27. Minhas PS, Liu L, Moon PK, Joshi AU, Dove C, Mhatre S, et al. Macrophage de novo NAD(+) synthesis specifies immune function in aging and inflammation. *Nat Immunol.* 2019; 20(1):50–63. Epub 20181126. <https://doi.org/10.1038/s41590-018-0255-3> PMID: 30478397; PubMed Central PMCID: PMC6768398.
28. Mor I, Cheung EC, Vousden KH. Control of glycolysis through regulation of PFK1: old friends and recent additions. *Cold Spring Harb Symp Quant Biol.* 2011; 76:211–6. Epub 20111117. <https://doi.org/10.1101/sqb.2011.76.010868> PMID: 22096029.
29. Tai W, He L, Zhang X, Pu J, Voronin D, Jiang S, et al. Characterization of the receptor-binding domain (RBD) of 2019 novel coronavirus: implication for development of RBD protein as a viral attachment inhibitor and vaccine. *Cell Mol Immunol.* 2020; 17(6):613–20. Epub 20200319. <https://doi.org/10.1038/s41423-020-0400-4> PMID: 32203189; PubMed Central PMCID: PMC7091888.
30. Lodge EK, Bell JD, Roloff EM, Hamilton KE, Louters LL, Looyenga BD. Pharmacologic inhibition of N-linked glycan trimming with kifunensine disrupts GLUT1 trafficking and glucose uptake. *Biochimie.* 2020; 174:18–29. Epub 20200413. <https://doi.org/10.1016/j.biochi.2020.04.001> PMID: 32298759; PubMed Central PMCID: PMC7282979.

31. Kuan SF, Byrd JC, Basbaum C, Kim YS. Inhibition of mucin glycosylation by aryl-N-acetyl- α -galactosaminides in human colon cancer cells. *Journal of Biological Chemistry*. 1989; 264(32):19271–7. [https://doi.org/10.1016/s0021-9258\(19\)47297-9](https://doi.org/10.1016/s0021-9258(19)47297-9) PMID: 2509474
32. Yoon WH, Park HD, Lim K, Hwang BD. Effect of O-glycosylated mucin on invasion and metastasis of HM7 human colon cancer cells. *Biochem Biophys Res Commun*. 1996; 222(3):694–9. Epub 1996/05/24. <https://doi.org/10.1006/bbrc.1996.0806> PMID: 8651907.
33. Iyer NV, Kotch LE, Agani F, Leung SW, Laughner E, Wenger RH, et al. Cellular and developmental control of O₂ homeostasis by hypoxia-inducible factor 1 alpha. *Genes Dev*. 1998; 12(2):149–62. <https://doi.org/10.1101/gad.12.2.149> PMID: 9436976; PubMed Central PMCID: PMC316445.
34. Peng H-L, Chang H-Y. Cloning of a human liver UDP-glucose pyrophosphorylase cDNA by complementation of the bacterial galU mutation. *FEBS Letters*. 1993; 329(1–2):153–8. [https://doi.org/10.1016/0014-5793\(93\)80213-e](https://doi.org/10.1016/0014-5793(93)80213-e) PMID: 8354390
35. Heesen S, Lehle L, Weissmann A, Aebi M. Isolation of the ALG5 locus encoding the UDP-glucose:dolichyl-phosphate glucosyltransferase from *Saccharomyces cerevisiae*. *Eur J Biochem*. 1994; 224(1):71–9. <https://doi.org/10.1111/j.1432-1033.1994.tb19996.x> PMID: 8076653.
36. Kumar R, Yang J, Larsen RD, Stanley P. Cloning and expression of N-acetylglucosaminyltransferase I, the medial Golgi transferase that initiates complex N-linked carbohydrate formation. *Proc Natl Acad Sci U S A*. 1990; 87(24):9948–52. <https://doi.org/10.1073/pnas.87.24.9948> PMID: 1702225; PubMed Central PMCID: PMC55291.
37. Swyryd EA, Seaver SS, Stark GR. N-(Phosphonacetyl)-l-Aspartate, a Potent Transition State Analog Inhibitor of Aspartate Transcarbamylase, Blocks Proliferation of Mammalian Cells in Culture. *Journal of Biological Chemistry*. 1974; 249(21):6945–50. [https://doi.org/10.1016/s0021-9258\(19\)42149-2](https://doi.org/10.1016/s0021-9258(19)42149-2) PMID: 4371054
38. Leban J, Kralik M, Mies J, Gassen M, Tentschert K, Baumgartner R. SAR, species specificity, and cellular activity of cyclopentene dicarboxylic acid amides as DHODH inhibitors. *Bioorg Med Chem Lett*. 2005; 15(21):4854–7. <https://doi.org/10.1016/j.bmcl.2005.07.053> PMID: 16143532.
39. Koutcher JA, Alfieri AA, Matei C, Meyer KL, Street JC, Martin DS. Effect of 6-aminonicotinamide on the pentose phosphate pathway: 31P NMR and tumor growth delay studies. *Magn Reson Med*. 1996; 36(6):887–92. <https://doi.org/10.1002/mrm.1910360611> PMID: 8946354.
40. Thomas AA, De Meese J, Le Huerou Y, Boyd SA, Romoff TT, Gonzales SS, et al. Non-charged thiamine analogs as inhibitors of enzyme transketolase. *Bioorg Med Chem Lett*. 2008; 18(2):509–12. Epub 2007/12/03. <https://doi.org/10.1016/j.bmcl.2007.11.098> PMID: 18182286.
41. Remels AH, Gosker HR, Verhees KJ, Langen RC, Schols AM. TNF-alpha-induced NF-kappaB activation stimulates skeletal muscle glycolytic metabolism through activation of HIF-1 alpha. *Endocrinology*. 2015; 156(5):1770–81. Epub 2015/02/25. <https://doi.org/10.1210/en.2014-1591> PMID: 25710281.
42. Wilson JE. Isozymes of mammalian hexokinase: structure, subcellular localization and metabolic function. *J Exp Biol*. 2003; 206(Pt 12):2049–57. <https://doi.org/10.1242/jeb.00241> PMID: 12756287.
43. Roberts DJ, Miyamoto S. Hexokinase II integrates energy metabolism and cellular protection: Acting on mitochondria and TORCing to autophagy. *Cell Death Differ*. 2015; 22(2):248–57. Epub 2014/10/17. <https://doi.org/10.1038/cdd.2014.173> PMID: 25323588; PubMed Central PMCID: PMC4291497.
44. Mathupala SP, Ko YH, Pedersen PL. Hexokinase II: cancer's double-edged sword acting as both facilitator and gatekeeper of malignancy when bound to mitochondria. *Oncogene*. 2006; 25(34):4777–86. Epub 2006/08/08. <https://doi.org/10.1038/sj.onc.1209603> PMID: 16892090; PubMed Central PMCID: PMC3385868.
45. Abu-Hamad S, Zaid H, Israelson A, Nahon E, Shoshan-Barmatz V. Hexokinase-I protection against apoptotic cell death is mediated via interaction with the voltage-dependent anion channel-1: mapping the site of binding. *J Biol Chem*. 2008; 283(19):13482–90. Epub 2008/03/01. <https://doi.org/10.1074/jbc.M708216200> PMID: 18308720.
46. Wise LM, Xi Y, Purdy JG. Hypoxia-Inducible Factor 1alpha (HIF1alpha) Suppresses Virus Replication in Human Cytomegalovirus Infection by Limiting Kynurenine Synthesis. *mBio*. 2021; 12(2). Epub 2021/03/23. <https://doi.org/10.1128/mBio.02956-20> PMID: 33758082; PubMed Central PMCID: PMC8092273.
47. Chen Y, Guillemin GJ. Kynurenine pathway metabolites in humans: disease and healthy States. *Int J Tryptophan Res*. 2009; 2:1–19. Epub 2009/10/08. <https://doi.org/10.4137/ijtr.s2097> PMID: 22084578; PubMed Central PMCID: PMC3195227.
48. Mandi Y, Vecsei L. The kynurenine system and immunoregulation. *J Neural Transm (Vienna)*. 2012; 119(2):197–209. Epub 2011/07/09. <https://doi.org/10.1007/s00702-011-0681-y> PMID: 21744051.
49. Ohtsubo K, Marth JD. Glycosylation in cellular mechanisms of health and disease. *Cell*. 2006; 126(5):855–67. <https://doi.org/10.1016/j.cell.2006.08.019> PMID: 16959566.

50. Jayaprakash NG, Surolia A. Role of glycosylation in nucleating protein folding and stability. *Biochem J.* 2017; 474(14):2333–47. Epub 2017/07/05. <https://doi.org/10.1042/BCJ20170111> PMID: 28673927.
51. Rudd PM, Elliott T, Cresswell P, Wilson IA, Dwek RA. Glycosylation and the immune system. *Science.* 2001; 291(5512):2370–6. <https://doi.org/10.1126/science.291.5512.2370> PMID: 11269318.
52. Marth JD, Grewal PK. Mammalian glycosylation in immunity. *Nat Rev Immunol.* 2008; 8(11):874–87. <https://doi.org/10.1038/nri2417> PMID: 18846099; PubMed Central PMCID: PMC2768770.
53. Liu Z, Pan Q, Ding S, Qian J, Xu F, Zhou J, et al. The interferon-inducible MxB protein inhibits HIV-1 infection. *Cell Host Microbe.* 2013; 14(4):398–410. Epub 20130919. <https://doi.org/10.1016/j.chom.2013.08.015> PMID: 24055605.
54. Brehin AC, Casademont I, Frenkiel MP, Julier C, Sakuntabhai A, Despres P. The large form of human 2',5'-Oligoadenylate Synthetase (OAS3) exerts antiviral effect against Chikungunya virus. *Virology.* 2009; 384(1):216–22. Epub 20081203. <https://doi.org/10.1016/j.virol.2008.10.021> PMID: 19056102.
55. Dafa-Berger A, Kuzmina A, Fassler M, Yitzhak-Asraf H, Shemer-Avni Y, Taube R. Modulation of hepatitis C virus release by the interferon-induced protein BST-2/tetherin. *Virology.* 2012; 428(2):98–111. Epub 20120420. <https://doi.org/10.1016/j.virol.2012.03.011> PMID: 22520941.
56. Hinz A, Miguet N, Natrajan G, Usami Y, Yamanaka H, Renesto P, et al. Structural basis of HIV-1 tethering to membranes by the BST-2/tetherin ectodomain. *Cell Host Microbe.* 2010; 7(4):314–23. <https://doi.org/10.1016/j.chom.2010.03.005> PMID: 20399176; PubMed Central PMCID: PMC2859121.
57. Goodwin CM, Xu S, Munger J. Stealing the Keys to the Kitchen: Viral Manipulation of the Host Cell Metabolic Network. *Trends Microbiol.* 2015. Epub 2015/10/07. <https://doi.org/10.1016/j.tim.2015.08.007> PMID: 26439298.
58. McArdle J, Schafer XL, Munger J. Inhibition of calmodulin-dependent kinase kinase blocks human cytomegalovirus-induced glycolytic activation and severely attenuates production of viral progeny. *J Virol.* 2011; 85(2):705–14. Epub 2010/11/19. doi: JVI.01557-10 [pii] <https://doi.org/10.1128/JVI.01557-10> PMID: 21084482; PubMed Central PMCID: PMC3019999.
59. Munger J, Bajad SU, Collier HA, Shenk T, Rabinowitz JD. Dynamics of the Cellular Metabolome during Human Cytomegalovirus Infection. *PLoS Pathog.* 2006; 2(12):e132. <https://doi.org/10.1371/journal.ppat.0020132> PMID: 17173481.
60. Radsak KD, Weder D. Effect of 2-deoxy-D-glucose on cytomegalovirus-induced DNA synthesis in human fibroblasts. *J Gen Virol.* 1981; 57(Pt 1):33–42. Epub 1981/11/01. <https://doi.org/10.1099/0022-1317-57-1-33> PMID: 6275020.
61. Combs JA, Monk CH, Harrison MAA, Norton EB, Morris CA, Sullivan DE, et al. Inhibiting cytomegalovirus replication through targeting the host electron transport chain. *Antiviral Res.* 2021; 194:105159. Epub 2021/08/15. <https://doi.org/10.1016/j.antiviral.2021.105159> PMID: 34390771; PubMed Central PMCID: PMC8446325.
62. Betsinger CN, Jankowski CSR, Hofstadter WA, Federspiel JD, Otter CJ, Jean Beltran PM, et al. The human cytomegalovirus protein pUL13 targets mitochondrial cristae architecture to increase cellular respiration during infection. *Proc Natl Acad Sci U S A.* 2021; 118(32). Epub 2021/08/05. <https://doi.org/10.1073/pnas.2101675118> PMID: 34344827; PubMed Central PMCID: PMC8364163.
63. Combs JA, Norton EB, Saifudeen ZR, Bentrup KHZ, Katakam PV, Morris CA, et al. Human Cytomegalovirus Alters Host Cell Mitochondrial Function during Acute Infection. *J Virol.* 2020; 94(2). Epub 2019/11/07. <https://doi.org/10.1128/JVI.01183-19> PMID: 31694945; PubMed Central PMCID: PMC6955246.
64. Codo AC, Davanzo GG, Monteiro LB, de Souza GF, Muraro SP, Virgilio-da-Silva JV, et al. Elevated Glucose Levels Favor SARS-CoV-2 Infection and Monocyte Response through a HIF-1 α /Glycolysis-Dependent Axis. *Cell metabolism.* 2020; 32(3):437–46.e5. Epub 2020/07/23. <https://doi.org/10.1016/j.cmet.2020.07.007> PMID: 32697943; PubMed Central PMCID: PMC7367032.
65. Kohnhorst CL, Kyoung M, Jeon M, Schmitt DL, Kennedy EL, Ramirez J, et al. Identification of a multienzyme complex for glucose metabolism in living cells. *J Biol Chem.* 2017; 292(22):9191–203. Epub 2017/04/21. <https://doi.org/10.1074/jbc.M117.783050> PMID: 28424264; PubMed Central PMCID: PMC5454101.
66. Schmitt DL, An S. Spatial Organization of Metabolic Enzyme Complexes in Cells. *Biochemistry.* 2017; 56(25):3184–96. Epub 2017/06/06. <https://doi.org/10.1021/acs.biochem.7b00249> PMID: 28580779; PubMed Central PMCID: PMC5574030.
67. Malaisse WJ, Zhang Y, Sener A. Enzyme-to-enzyme channeling in the early steps of glycolysis in rat pancreatic islets. *Endocrine.* 2004; 24(2):105–9. Epub 2004/09/07. <https://doi.org/10.1385/ENDO:24:2:105> PMID: 15347834.
68. Ramana CV, Chatterjee-Kishore M, Nguyen H, Stark GR. Complex roles of Stat1 in regulating gene expression. *Oncogene.* 2000; 19(21):2619–27. Epub 2000/06/13. <https://doi.org/10.1038/sj.onc.1203525> PMID: 10851061.

69. Raymonda MH, Ciesla JH, Monaghan M, Leach J, Asantewaa G, Smorodintsev-Schiller LA, et al. Pharmacologic profiling reveals lapatinib as a novel antiviral against SARS-CoV-2 in vitro. *Virology*. 2021; 566:60–8. Epub 2021 1127. <https://doi.org/10.1016/j.virol.2021.11.008> PMID: 34871905; PubMed Central PMCID: PMC8626825.
70. Yu D, Silva MC, Shenk T. Functional map of human cytomegalovirus AD169 defined by global mutational analysis. *Proc Natl Acad Sci U S A*. 2003; 100(21):12396–401. Epub 2003/10/02. <https://doi.org/10.1073/pnas.1635160100> PMID: 14519856; PubMed Central PMCID: PMC218769.
71. O'Connor CM, Shenk T. Human cytomegalovirus pUS27 G protein-coupled receptor homologue is required for efficient spread by the extracellular route but not for direct cell-to-cell spread. *J Virol*. 2011; 85(8):3700–7. Epub 20110209. <https://doi.org/10.1128/JVI.02442-10> PMID: 21307184; PubMed Central PMCID: PMC3126124.
72. Lindenbach BD. Measuring HCV infectivity produced in cell culture and in vivo. *Methods Mol Biol*. 2009; 510:329–36. https://doi.org/10.1007/978-1-59745-394-3_24 PMID: 19009272.
73. Rodriguez-Sanchez I, Schafer XL, Monaghan M, Munger J. The Human Cytomegalovirus UL38 protein drives mTOR-independent metabolic flux reprogramming by inhibiting TSC2. *PLoS Pathog*. 2019; 15(1):e1007569. Epub 2019/01/25. <https://doi.org/10.1371/journal.ppat.1007569> PMID: 30677091; PubMed Central PMCID: PMC6363234.
74. Zhu H, Shen Y, Shenk T. Human cytomegalovirus IE1 and IE2 proteins block apoptosis. *J Virol*. 1995; 69(12):7960–70. Epub 1995/12/01. <https://doi.org/10.1128/JVI.69.12.7960-7970.1995> PMID: 7494309; PubMed Central PMCID: PMC189741.
75. Silva MC, Yu QC, Enquist L, Shenk T. Human cytomegalovirus UL99-encoded pp28 is required for the cytoplasmic envelopment of tegument-associated capsids. *J Virol*. 2003; 77(19):10594–605. Epub 2003/09/13. <https://doi.org/10.1128/jvi.77.19.10594-10605.2003> PMID: 12970444; PubMed Central PMCID: PMC228509.
76. Munger J, Yu D, Shenk T. UL26-deficient human cytomegalovirus produces virions with hypophosphorylated pp28 tegument protein that is unstable within newly infected cells. *J Virol*. 2006; 80(7):3541–8. Epub 2006/03/16. <https://doi.org/10.1128/JVI.80.7.3541-3548.2006> PMID: 16537622; PubMed Central PMCID: PMC1440364.
77. Hsiao T, Conant D, Rossi N, Maures T, Waite K, Yang J, et al. Inference of CRISPR Edits from Sanger Trace Data. *BioRxiv*. 2019. <https://doi.org/10.1101/251082>
78. DeVito SR, Ortiz-Riano E, Martinez-Sobrido L, Munger J. Cytomegalovirus-mediated activation of pyrimidine biosynthesis drives UDP-sugar synthesis to support viral protein glycosylation. *Proc Natl Acad Sci U S A*. 2014; 111(50):18019–24. Epub 2014/12/05. <https://doi.org/10.1073/pnas.1415864111> PMID: 25472841; PubMed Central PMCID: PMC4273352.
79. Pang Z, Chong J, Zhou G, de Lima Morais DA, Chang L, Barrette M, et al. MetaboAnalyst 5.0: narrowing the gap between raw spectra and functional insights. *Nucleic Acids Res*. 2021; 49(W1):W388–W96. <https://doi.org/10.1093/nar/gkab382> PMID: 34019663; PubMed Central PMCID: PMC8265181.
80. Sun S, Hu Y, Ao M, Shah P, Chen J, Yang W, et al. N-GlycositeAtlas: a database resource for mass spectrometry-based human N-linked glycoprotein and glycosylation site mapping. *Clin Proteomics*. 2019; 16:35. Epub 20190907. <https://doi.org/10.1186/s12014-019-9254-0> PMID: 31516400; PubMed Central PMCID: PMC6731604.
81. Huang J, Wu M, Zhang Y, Kong S, Liu M, Jiang B, et al. OGP: A Repository of Experimentally Characterized O-Glycoproteins to Facilitate Studies on O-Glycosylation. *Genomics Proteomics Bioinformatics*. 2021. Epub 20210210. <https://doi.org/10.1016/j.gpb.2020.05.003> PMID: 33581334.